Local Earthquake Tomography in the Tjörnes Fracture Zone (North Iceland)

Claudia Abril[1,1,1], Ari Tryggvason[2,2,2], Ólafur Gudmundsson[3,3,3], and Rebekka Steffen[4,4,4]

[1]Icelandic Meteorological Office
[2]Uppsala University
[3]Unknown
[4]Lantmäteriet

November 30, 2022

Abstract

Local earthquake tomography has been carried out in the Tjörnes Fracture Zone. This transform region connects the Mid-Atlantic Ridge with the Northern Volcanic Zone in Iceland in a mostly offshore area. The challenge to record seismic information in this area was the motivation for the North ICeland Experiment (NICE). Fourteen ocean-bottom seismometers and eleven on-land stations were installed in the project and operated simultaneously with the permanent Icelandic seismic network (SIL) during summer 2004. Data from the experiment were used to estimate P- and S-wave crustal velocities. Also, the Bouguer gravity anomaly was derived for comparison with the tomographic results. Upper-crustal velocities are found to be relatively low in the offshore region. In particular, low velocities are mapped along the Húsavík-Flatey Fault, where a more confined negative gravity anomaly and a sedimentary basin are found. Low velocities are also mapped along the Grímsey Oblique Rift and in a zone connecting these two main lineaments north of Skjálfandi Bay. The northern half of the aseismic Grímsey Shoal appears as a fast anomaly. Furthermore, localized high-velocity anomalies are found beneath northern Trölaskagi and Flateyjarskagi Peninsulas, where bedrock dates from Upper and Middle Miocene (10-15 Ma). Regions of low Vp/Vs ratio are mapped at depth along the main lineaments. Low velocities along the lineaments are interpreted as due to fracturing extending into the middle crust, while fast upper-crustal velocities beneath Tertiary formations are associated with relic volcanoes. Low Vp/Vs ratios along the lineaments are interpreted as due to the presence of supercritical fluids.

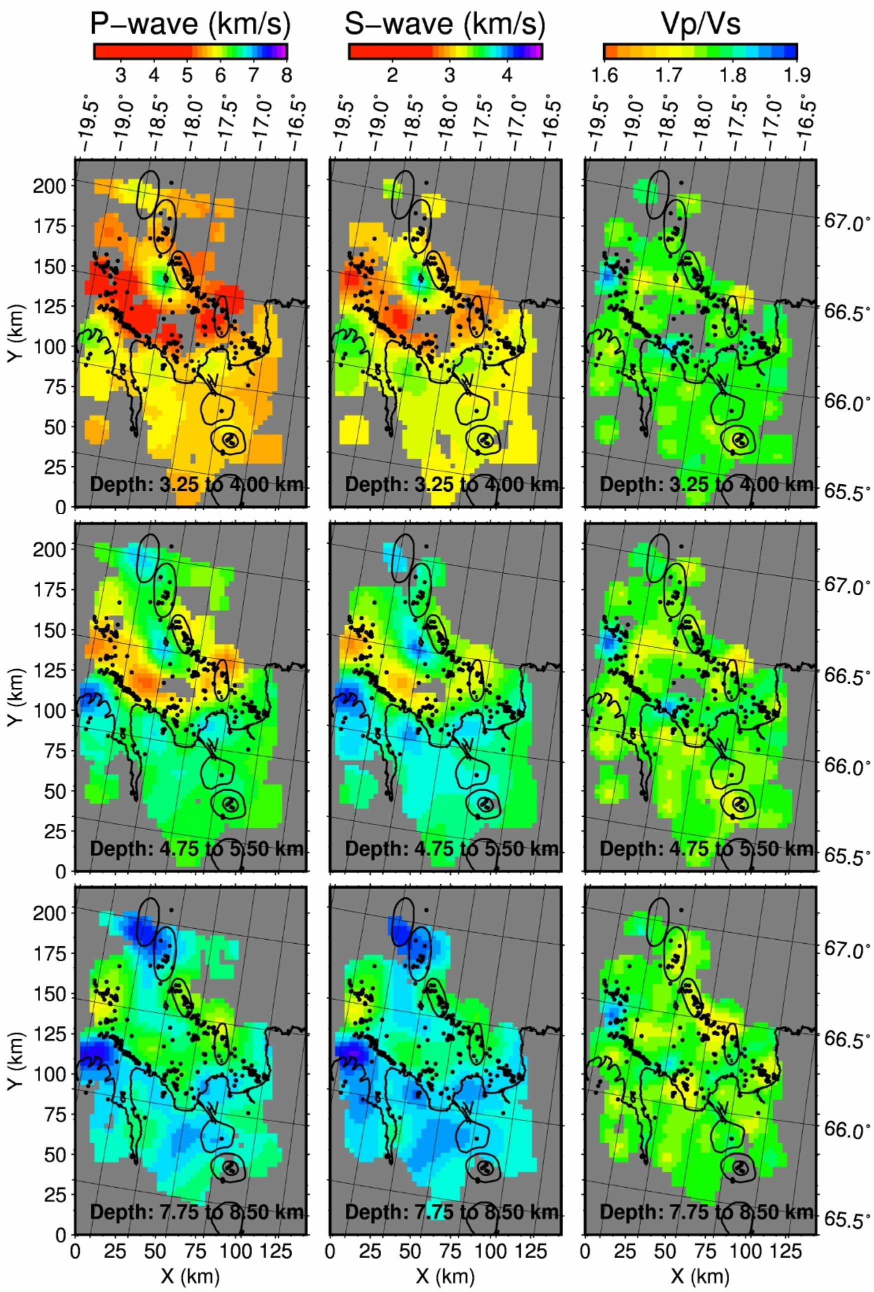
P−wave (km/s)
3 4 5 6 7 8
S−wave (km/s)
2 3 4
Vp/Vs
1.6 1.7 1.8 1.9
−19.5° −19.0° −18.5° −18.0° −17.5° −17.0° −16.5°
67.0° 66.5° 66.0° 65.5°
Y (km)
0 25 50 75 100 125 150 175 200
Depth: 3.25 to 4.00 km
Depth: 4.75 to 5.50 km
Depth: 7.75 to 8.50 km
X (km)
0 25 50 75 100 125

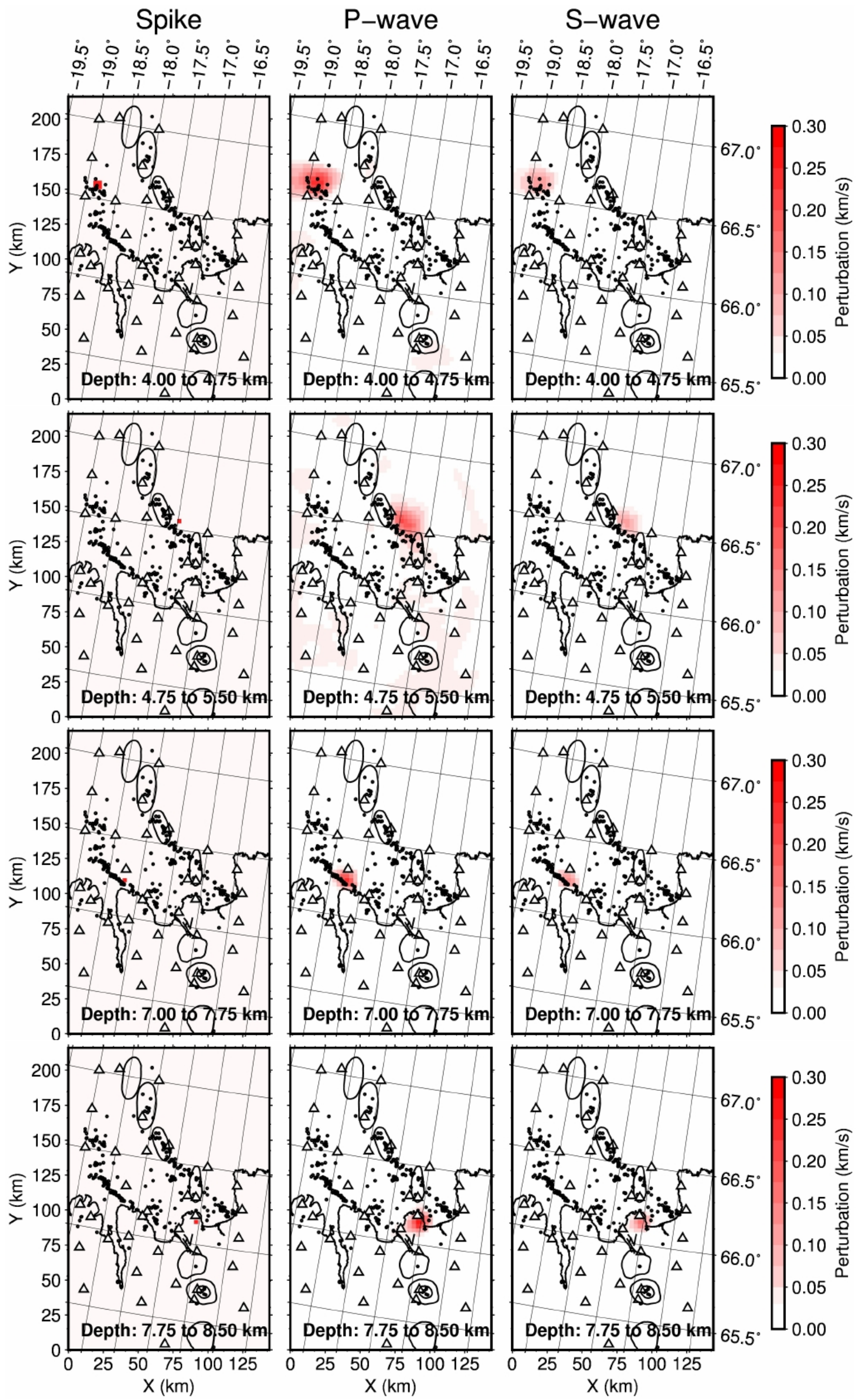
Spike
P−wave
S−wave
Depth: 4.00 to 4.75 km
Depth: 4.75 to 5.50 km
Depth: 7.00 to 7.75 km
Depth: 7.75 to 8.50 km
Y (km)
X (km)
Perturbation (km/s)

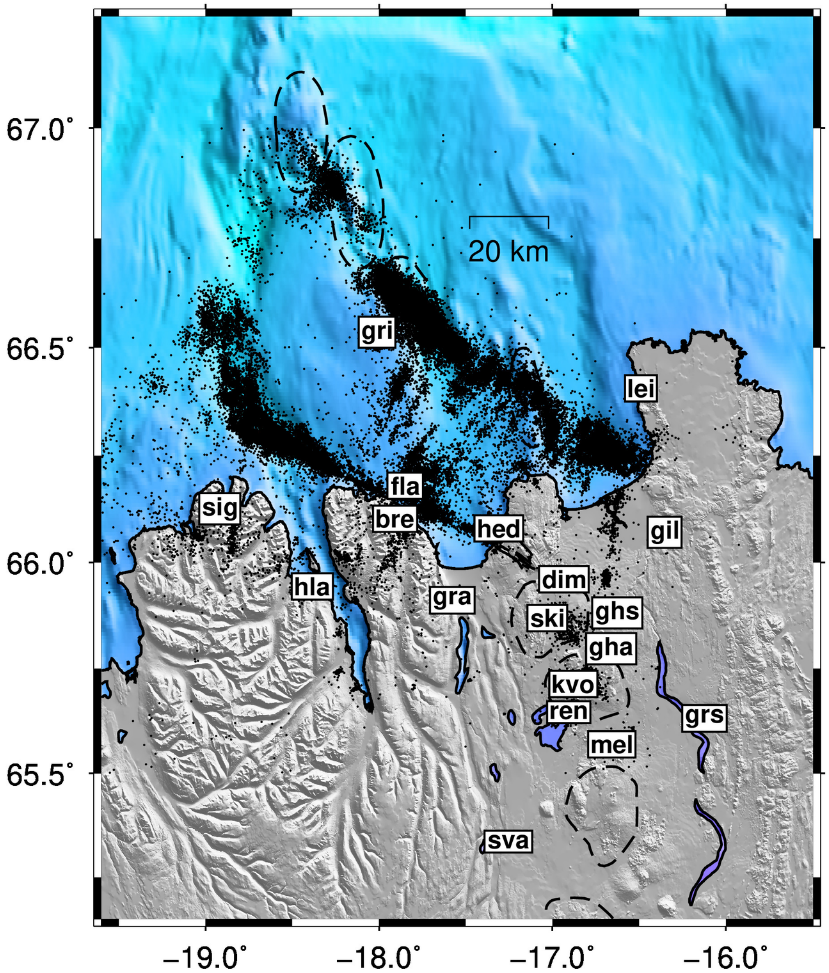
67.0˚
66.5˚
66.0˚
65.5˚
−19.0˚
−18.0˚
−17.0˚
−16.0˚
20 km
gri
lei
fla
sig
bre
hed
gil
hla
gra
dim
ski
ghs
gha
kvo
ren
grs
mel
sva

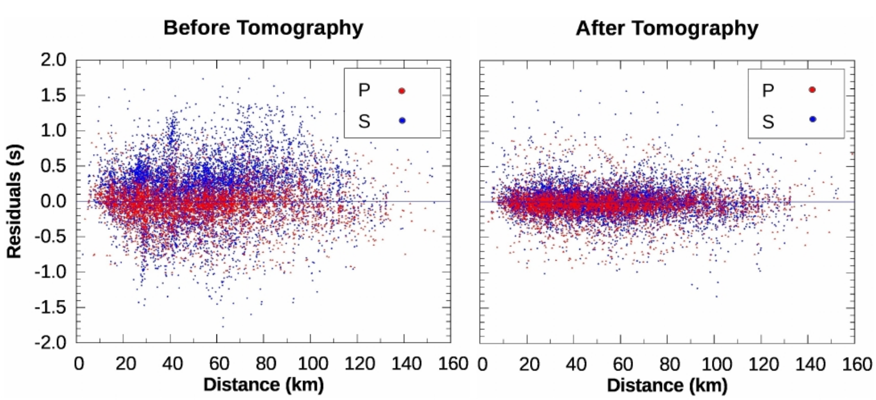
Before Tomography
After Tomography
Residuals (s)
Distance (km)
P
S
2.0
1.5
1.0
0.5
0.0
-0.5
-1.0
-1.5
-2.0
0
20
40
60
80
100
120
140
160

(a) (b)

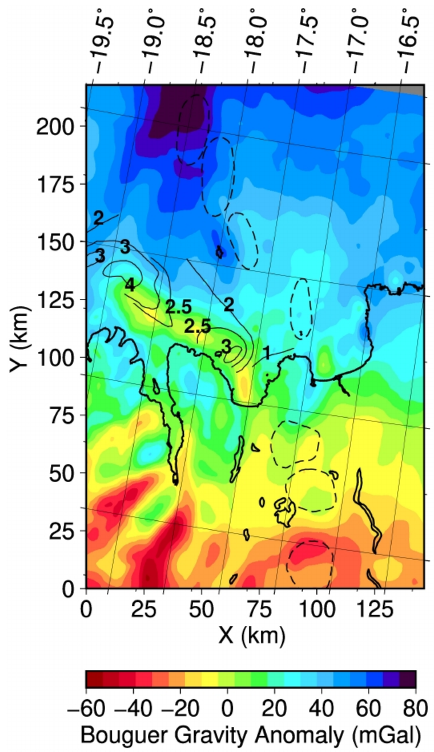

−19.5°
−19.0°
−18.5°
−18.0°
−17.5°
−17.0°
−16.5°
Y (km)
X (km)
Bouguer Gravity Anomaly (mGal)

(a)

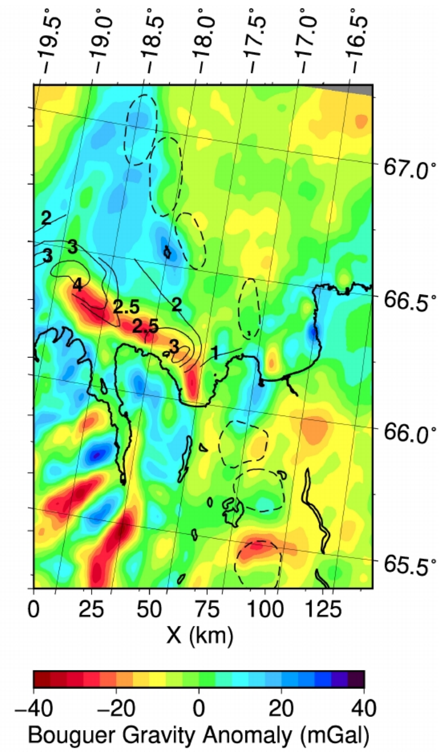

−19.5°
−19.0°
−18.5°
−18.0°
−17.5°
−17.0°
−16.5°
67.0°
66.5°
66.0°
65.5°
X (km)
Bouguer Gravity Anomaly (mGal)

(b)

Local Earthquake Tomography in the Tjörnes Fracture Zone (North Iceland)

C. Abril[1,2], A. Tryggvason[2], Ó. Gudmundsson[2], R. Steffen[1,3]

[1]Department of Earth Sciences, Uppsala University, Uppsala, Sweden
[2]Icelandic Meteorological Office - IMO, Reykjavík, Iceland
[3]Lantmäteriet, Gävle, Sweden

Key Points:

- Local earthquake tomography maps a low-velocity anomaly along the Húsavík-Flatey Fault.
- A curvilinear Bouguer gravity low coincides with the low-velocity anomaly.
- Low Vp/Vs ratios are found at 5-10 km depth beneath the main lineaments of the Tjörnes Fracture Zone.

Corresponding author: Claudia Abril, `claudia@vedur.is`

Abstract

Local earthquake tomography has been carried out in the Tjörnes Fracture Zone. This transform region connects the Mid-Atlantic Ridge with the Northern Volcanic Zone in Iceland in a mostly offshore area. The challenge to record seismic information in this area was the motivation for the North ICeland Experiment (NICE). Fourteen ocean-bottom seismometers and eleven on-land stations were installed in the project and operated simultaneously with the permanent Icelandic seismic network (SIL) during summer 2004. Data from the experiment were used to estimate P- and S-wave crustal velocities. Also, the Bouguer gravity anomaly was derived for comparison with the tomographic results. Upper-crustal velocities are found to be relatively low in the offshore region. In particular, low velocities are mapped along the Húsavík-Flatey Fault, where a more confined negative gravity anomaly and a sedimentary basin are found. Low velocities are also mapped along the Grímsey Oblique Rift and in a zone connecting these two main lineaments north of Skjálfandi Bay. The northern half of the aseismic Grímsey Shoal appears as a fast anomaly. Furthermore, localized high-velocity anomalies are found beneath northern Tröllaskagi and Flateyjarskagi Peninsulas, where bedrock dates from Upper and Middle Miocene (10-15 Ma). Regions of low Vp/Vs ratio are mapped at depth along the main lineaments. Low velocities along the lineaments are interpreted as due to fracturing extending into the middle crust, while fast upper-crustal velocities beneath Tertiary formations are associated with relic volcanoes. Low Vp/Vs ratios along the lineaments are interpreted as due to the presence of supercritical fluids.

1 Introduction

The Tjörnes Fracture Zone (TFZ) is a transform zone that connects the Kolbeinsey Ridge (KR) with the Northern Volcanic Zone (NVZ) of Iceland. The TFZ has two main semi-parallel structures oriented SE-NW: the Húsavík Flatey Fault (HFF) and the Grímsey Oblique Rift (GOR). Additionally, the KR continues to the south as the Eyjafjarðaráll Rift (ER) on the western border of the TFZ. Together these parts of the TFZ demark the Tjörnes Microplate (TM) (see Figure 1). The HFF, the GOR and the ER encompass most of the seismicity in the region (Figure 2).

The HFF is a WNW-striking, right-lateral strike-slip fault that extends from the Þeistareykir fissure swarm in the NVZ to the southern end of the ER. The eastern part of the HFF is a set of subparallel faults located on land on the Tjörnes Peninsula. The cen-

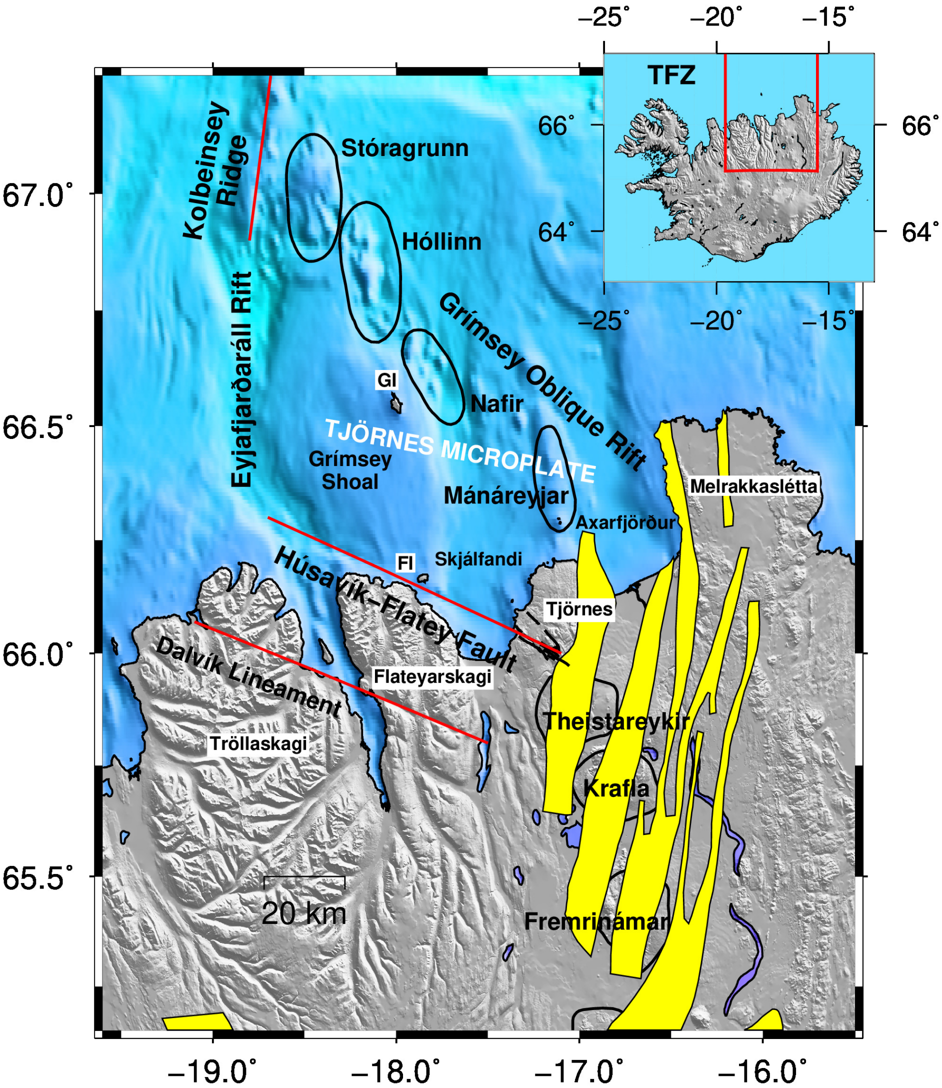

Figure 1: Map of Northern Iceland. The Tjörnes Fracture Zone connects the Kolbeinsey Ridge with the Northern Volcanic Zone and its volcanic centers (Þeistareykir, Krafla and Fremrinámar are shown here). The main tectonic structures of the TFZ are the Húsavík-Flatey Fault, the volcanic centers in the Grímsey Oblique Rift and the Eyjafjarðaráll Basin. An outline of the suggested Dalvík Lineament is also shown. Flatey (FI) and Grímsey (GI) Islands are presented for geographic reference.

tral and western parts are located offshore (Figure 1). The ER is a pull-apart basin characterized by a semi-symmetric pattern of normal faulting on a north-striking axis [*Gunnarsson*, 1998]. The basin widens to the south near the HFF in a corridor $\sim$ 20 km wide. Evidence for recent volcanism is scarce [*Einarsson*, 2008]. The ER connects to the GOR

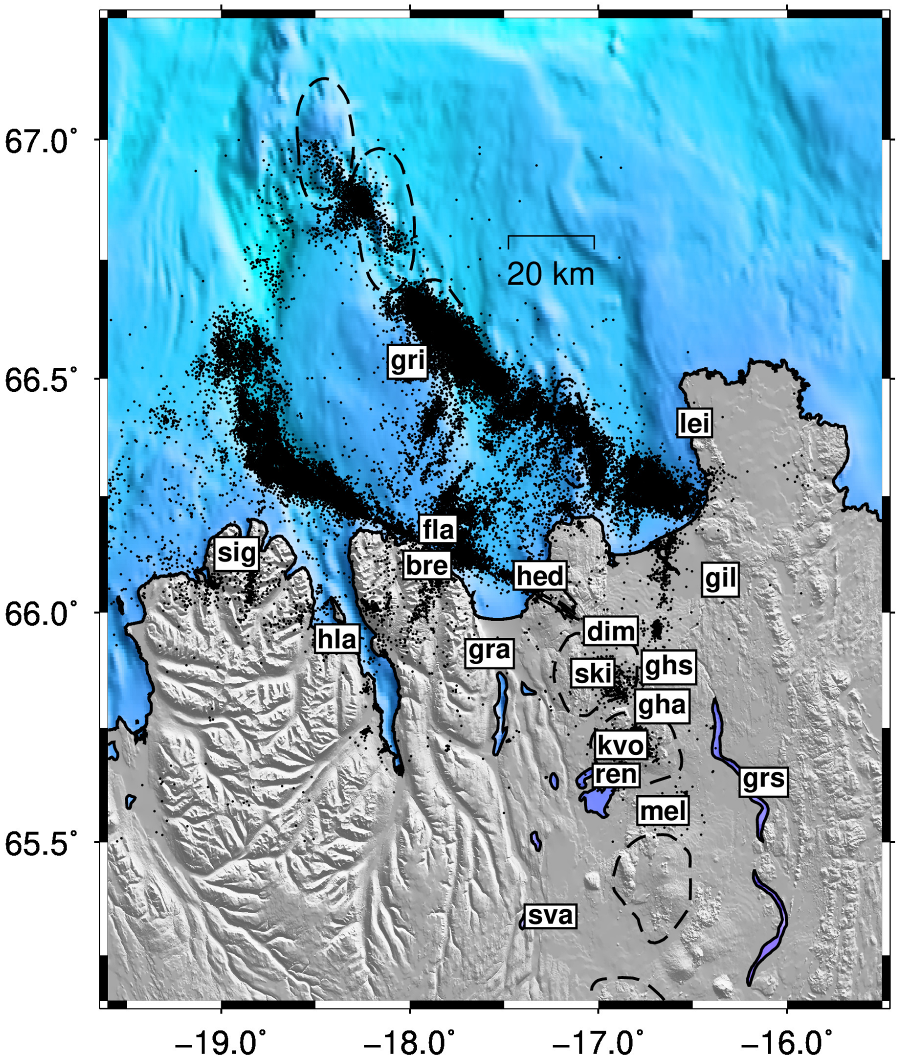

Figure 2: Seismicity in Northern Iceland recorded by the SIL network from 1993-2017 (black dots) and the distribution of SIL stations during the NICE experiment (summer 2004). Station names are presented in white boxes.

in the north, a lineament that is subparallel to the HFF and composed of four volcanic systems arranged *en echelon* and oriented NS to NNW-SSE [*Magnúsdóttir et al.*, 2015; *Rögnvaldsson et al.*, 1998], and transverse (NNE striking) strike-slip faults. The GOR connects to the Krafla fissure swarm at its eastern end. Evidence of recent volcanism in the GOR is abundant. The last eruptive activity occurred within the Mánareyar volcanic system in 1867-1868 [*Sæmundsson*, 1973].

Other lineaments also associated with the TFZ have less frequent earthquakes compared to the HFF and the GOR. One of them is the Dalvík Lineament (DL), associated with seismicity located south of the HFF, including some of the largest historic earthquakes in the TFZ. For example, the 1934 M=6.3 and the 1963 M=7.0 earthquakes occurred there [*Stefansson*, 1979]. Transverse lineaments that connect the HFF with the GOR have previously been suggested by *Rögnvaldsson et al.* [1998] and later supported by the earthquake relocations by *Abril et al.* [2018].

Some studies have used the SIL data to describe the crustal structure of the Northern Iceland. *Darbyshire et al.* [2000] generated teleseismic receiver functions at broadband stations of the SIL network. In general, receiver functions evidenced strong lateral heterogeneity in the crustal structure of the region. A crustal thickness of 20-22 km was estimated to the southeast near the Northern Volcanic Zone (stations REN and GRA), while a thicker crust of 25-30 km was modeled for stations GIL and SIG. A thinner crust of about 16 km was reported for the insular area (GRI). *Riedel et al.* [2005] performed a travel-time inversion using data from the SIL catalog. Assuming a maximum crustal velocity of 7.4 km/s, the crustal thickness was estimated to be 20 km at HFF and 8 km at the GOR.

As most of the TFZ is located offshore, available seismological and geological data collected on land provide limited information. However, some studies have collected and/or used offshore information about the TFZ. *Gunnarsson* [1998] reported thick sediments ($\sim<$ 4 km) along the HFF and around the ER, based on data from several campaigns of seismic reflection acquisition. *Magnúsdóttir et al.* [2015] used multi-beam bathymetry and high-resolution seismic reflection data (CHIRP) to study the area arround the Nafir volcanic system in the GOR. Correlation with tephrochronology from the sediment core MD99-2275 near Grímsey Island provided evidence of postglacial tectonic and volcanic activity along the lineament [*Søndergaard*, 2010; *Gudmundóttir*, 2010].

The North ICeland Experiment (NICE) was a temporary deployment of on-land and offshore seismological instruments to record data simultaneosly with the SIL network during the summer of 2004. The main purpose was to resolve the subsurface structure of the TFZ and study the transition from the Icelandic crust to more typical oceanic crust near the southern end of the Kolbeinsey Ridge [*Riedel et al.*, 2006]. In addition, to the seismological deployment, bathymetric mapping was performed, improving the resolution of previously available data. Structures in between Hóllinn and Stóragrunn volcanoes in the

GOR were revealed. *Hensch et al.* [2008] identified and located three earthquake swarms that occurred during the NICE deployment. Location of those swarms together with five swarms previously recorded by the SIL network suggested two different physical mechanisms: Magma propagation for the purely volcanic swarms, and hydrothermal activity and/or tectonic processes for swarms located outside the volcanic centers.

Here we analyze data from the NICE project further in order to study the TFZ. We present the results of Local Earthquake Tomography (LET) using 500 events (earthquakes and explosions) recorded during the span of the project. We also estimate the Bouguer gravity anomaly in the region for comparison with the tomographic results.

2 Data

The seismicity of the TFZ has been monitored with the SIL network since 1993 [*Bodvarsson et al.*, 1996; *Bödvarsson et al.*, 1999], recording more than 85.000 earthquakes in Northern Iceland. Earthquakes are monitored by stations located on the Icelandic coast, one station on Grímsey Island and one on Flatey Island (see Figure 2). The station distribution of the SIL network on-land renders locations of offshore earthquakes in the TFZ inaccurate. A large azimuthal gap, often grater than 180^o, affects the epicenter's estimate and large distances to the nearest stations (often exceeding 10 km) do not allow a precise estimate of focal depth [*Hensch et al.*, 2013]. This uncertainty in location parameters affects the resolution of tomographic studies using only the SIL catalog. Additionally, the sparse distribution of the SIL stations only allows illumination of the crust at depths from 7 to 12 km [*Riedel et al.*, 2005].

During the NICE project, 14 ocean-bottom seismometers (OBS) and 11 land stations were deployed in the summer of 2004 to operate simultaneously with the SIL network and record the seismicity of northern Iceland (see Figure 3). 16 explosions of 22.8-45.6 kg dynamite were fired in the water column and recorded [*Riedel et al.*, 2006]. They provided ray-paths in areas of the northern TFZ that are seismically quiet. The temporary station distribution extended the coverage area of the SIL network, which allows more accurate locations of the offshore seismicity and, in particular for earthquake tomography, illuminating also the upper-most crust, which was not covered by the SIL network alone.

A waveform database was created with data from the NICE and the SIL networks recorded during the simultaneous deployment, in order to facilitate a joint analysis and

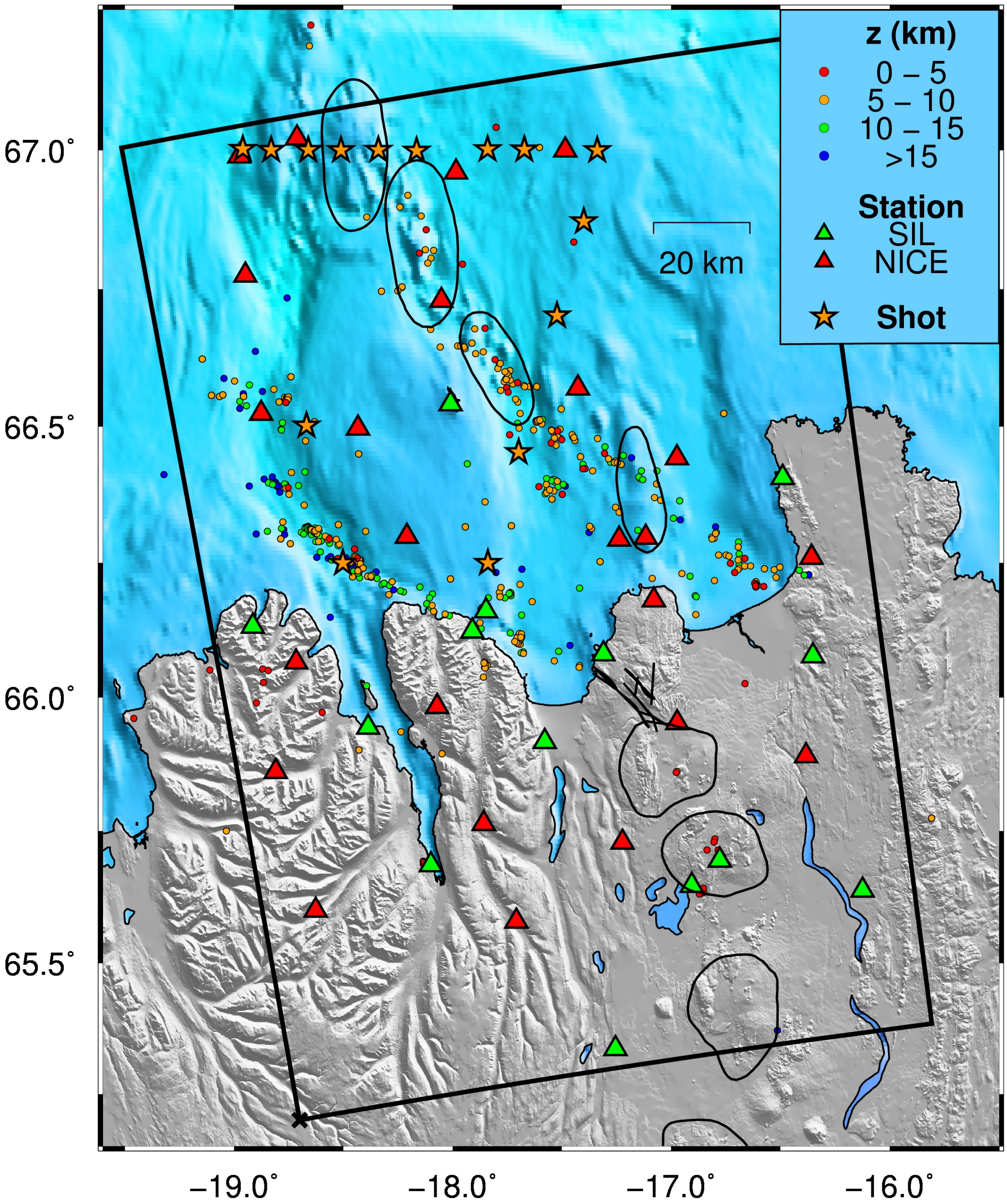

Figure 3: Distribution of seismic stations during the NICE experiment. Green triangles are the permanent SIL network stations. Red triangles are OBSs and additional on-land stations installed for the experiment. 484 earthquakes (black dots) together with the 16 shots (yellow stars) fired during the experiment were used in the LET. Earthquake locations are those estimated using the manual picking of P- and S-wave arrivals in SEISAN. The black rectangle outlines the study area. This is the area that will be used to present results in this paper, using a Cartesian coordinate system with origin in the southwestern corner of the black box (marked with a black cross).

phase picking. Continuous records of the NICE stations, after correction of the OBS data for clock drift [*Riedel et al.*, 2006], were converted from the GSE (Global Seismic Exchange) to the SEISAN format [*Havskov and Ottemöller*, 1999]. Independently, waveforms in the SIL catalog of earthquakes located in Northern Iceland were converted from SIL to SEISAN format. All the records were re-sampled to 100 Hz.

From the set of more than 1000 earthquakes used by *Hensch et al.* [2008], we selected a subset of 484 earthquakes and the 16 explosions (see Figure 3) such that geographical spread was maximized. Arrival times of the selected earthquakes were manually picked using SEISAN [*Havskov and Ottemöller*, 1999]. We recognized multiple P- and S-wave arrivals in some records, where we chose to pick the first arrival of each kind without distinguishing their specific ray-path geometry (direct or refracted). The final result of manual picking was a database of approximately 5500 P-wave arrivals and 7000 S-wave arrivals, that was used as input for the LET.

To locate earthquakes with the manual picks, we used the velocity model currently used for earthquake location of events in north Iceland in the SIL catalog. This model is an average one-dimensional (1-D) velocity model estimated by *Riedel et al.* [2005] using travel-time inversion (see Figure 4). A constant Vp/Vs ratio of 1.78 is assumed for this model, corresponding to the average value estimated by *Riedel et al.* [2005].

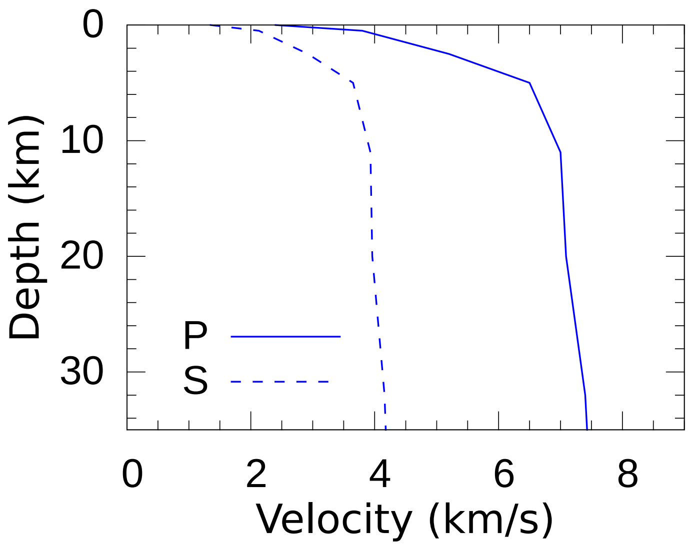

Figure 4: 1-D velocity model [*Riedel et al.*, 2005] used for initial earthquake location after manual picking of arrivals using SEISAN.

3 Local Earthquake Tomography (LET)

We used the program PStomo_{eq} to carry out the LET [*Tryggvason*, 1998; *Tryggvason et al.*, 2002]. PStomo_{eq} performs a simultaneous inversion for P- and S-wave velocity structure and the hypocentral parameters of local earthquakes. Controlled sources with fixed locations may be used as well [*Tryggvason*, 1998]. Travel times in PStomo_{eq} are computed with the *time3d* finite-difference algorithm [*Podvin and Lecomte*, 1991; *Tryggvason and Bergman*, 2006], which computes the time field from a source (or station) to all cells in the model. The algorithm is an application of Huygens' principle using a first order approximation of the Eikonal equation. The travel times to all receivers (or sources) are computed from the resulting time field and ray tracing is performed backwards perpendicular to the isochrons [*Hole*, 1992]. In the first step, the algorithm solves for only hypocentral parameters and then projects them out of the joint problem using the decomposition method by *Pavlis and Booker* [1980]. Slowness perturbations are determined with the conjugate gradient solver *LSQR*, that is well suited for solving large and sparse systems of linear equations [*Paige and Saunders*, 1982]. The tomography iteratively maps travel-time anomalies into slowness perturbations along ray paths such that new ray paths are computed in each iteration.

3.1 Starting Velocity Model and Inversion Procedure

The primary role of the starting model and initial earthquake locations is to provide ray-paths that are reasonably close to the true ones, avoiding that the linearized LET scheme will be trapped in a local minimum. Initial earthquake locations were estimated using the 1-D velocity model by *Riedel et al.* [2005] (see Figure 4), and we also used that model as a starting model for the LET. It resulted in stable 3-D velocity models and reduction of the root-mean-square (RMS) of travel-time residuals with each iteration. Several other starting models were also tested, 1D models but also simple 2D and 3D models accounting for i.e. the large variations in crustal thickness in the area. The crustal thickness varies from 26 km west of the Northern Volcanic Zone [*Menke et al.*, 1998], to 16 km underneath Grímsey Island [*Darbyshire et al.*, 2000] and 7.5 km beneath the Kolbeinsey Ridge [*Kodaira et al.*, 1997]. However, none of these models provided better final 3D P- and S-wave models in terms of RMS data fit. Thus, for simplicity we chose to use the 1D starting P- and S-wave models with a constant Vp/Vs ratio. Model cells of 0.75 km thickness and 3 km width in the horizontal were used in both models. Both larger and smaller cells were tested, but this discretization in combination with the applied model regularization appeared to reflect the model fidelity supported by the data.

3.2 Model Regularization

Regularization was applied in the inversion to minimize model artifacts [*Aster et al.*, 2005]. Smooth models were favored by pushing the Laplacian of the velocity models towards zero. Similarly, large Vp/Vs ratio variations were avoided by penalizing large deviations from the average value of 1.78. Weighting parameters controlled the two types of regularization, and their values were chosen following the L-curve test, mapping the trade-off between model roughness and data misfit. Model roughness was defined as the RMS of the velocity model, used as a weight for the cell's value of the ray coverage (total length of ray paths sections crossing the cell).

For the final inversion, the damping was gradually reduced in each iteration. The end value of the weighting factor of the Laplacian was 50, which is a good compromise of data fit and model roughness. We choose the Vp/Vs damping value as 5, below which the variation in Vp/Vs ratio results in models with unnecessary complicated Vp/Vs ratio variation.

3.3 Residuals and RMS

The LET reduced the travel-time residuals of P- and S-wave arrivals compared to the initial 1D model. Residuals before and after the LET are shown in Figure 5. Note that all events are initially relocated in the starting model. Residuals for S-wave arrival times (blue) tend to be bigger than those for P-waves (red) which may reflect that S-wave arrivals are more difficult to determine by manual picking. At the same time, the S-wave residuals are expected to be larger than the P-wave residuals as their travel times are longer. Figure 5 (a) also indicates that the P-wave residuals are fairly well centered on zero, suggesting that the starting model is unbiased. The S-wave residuals, on the other hand, are slightly biased to the positive side suggesting that the S-wave starting model is slightly slow. Figure 5 (b) shows residuals after the LET in the final 3-D velocity models. The width of the residual distribution (one standard deviation) is significantly reduced by the tomography from 0.28 s to 0.20 s (29% reduction) for the P-waves and from 0.47 s to 0.21 s (55%) for the S-waves. The mean value of the distribution is shifted towards zero, from -0.03 s to 0.01 s for P-waves, and from 0.17 to 0.02 s for S-waves. The RMS reduction of the data misfit after each iteration is presented in Figure 6. There is no reduction of the P-wave residual until the third iteration, which reflects the coupling of the P- and S-wave models in the earthquake locations. The bias in the starting S-wave model likely prevents the P-wave data fit to decrease before the bias in the S-wave model is reduced.

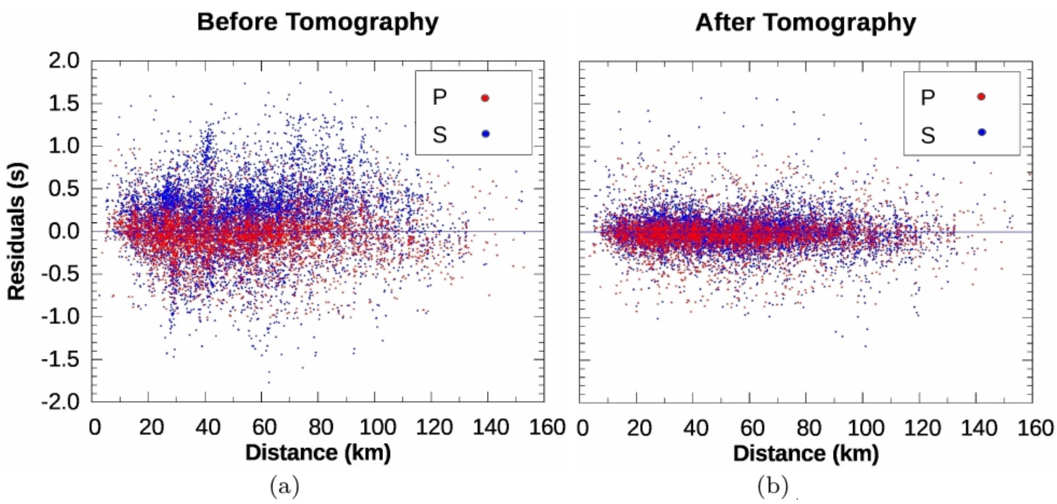

Figure 5: Residuals of P- (red dots) and S-wave (blue dots) arrival times (a) before LET and (b) after LET.

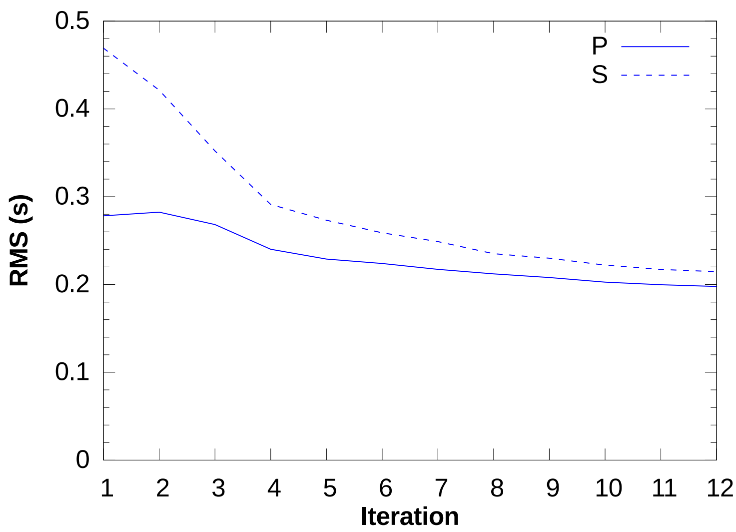

Figure 6: RMS reduction of P- (solid line) and S-wave (dashed line) data through the tomography schedule. The RMS data misfit is reduced by 29% for P-waves and 55% for S-waves.

3.4 Model Appraisal

Figure 7 shows the ray coverage through the models. The map view shows good horizontal ray coverage in the marine parts of the study area south of Grímsey. Ray coverage is predominantly subvertical in the top 3 to 4 km, and rays are abundant down to 15 km depth. Different tests have been carried out to appraise the model. Initially, a checkerboard test contributed to a general idea about the resolution of the final 3-D velocity model (not shown). This was followed up by spike tests to assess resolution length in selected areas. In the end, some of the main features of the final models were tested using hypothesis tests (see results in the Section 4.1). Map views shown in this and the following sections are restricted to the study area, represented by the black rectangle drawn in Figure 3. Cartesian coordinates are used as the reference coordinate system.

3.4.1 Spike Test

A spike test was carried out at some selected positions of the study area. This test helped to estimate resolution of the final velocity model and demonstrated smearing effects in the peripheral regions of the study area. A one-cell spike was used to perturb an averaged version of the final velocity model. Synthetic travel times were generated using the perturbed model, and afterwards those data were inverted to examine how well the spikes were recovered. Resolution was estimated by measuring the half width of the recovered anomaly (by half width we mean the full, double sided width between the points where the anomaly reaches half its maximum value). Results are presented in Figure 8. The region with the highest resolution is the central area of the TFZ near Flatey Island, and at the tip of the Tjörnes Peninsula in between the eastern part of HFF and the GOR, at a depth of $\sim$ 5 km. Resolution length in these regions is estimated to be 11 km in the horizontal directions and 4 km in depth. The recovered spike in the ER is broader than in the central TFZ, estimating a horizontal resolution of $\sim$ 20 km and a vertical resolution of $\sim$ 6 km. Some smearing is evident in the spike test. The recovered spike in the GOR is anisotropically broader than in the central TFZ, showing a pronounced elongation in the direction parallel to the lineament.

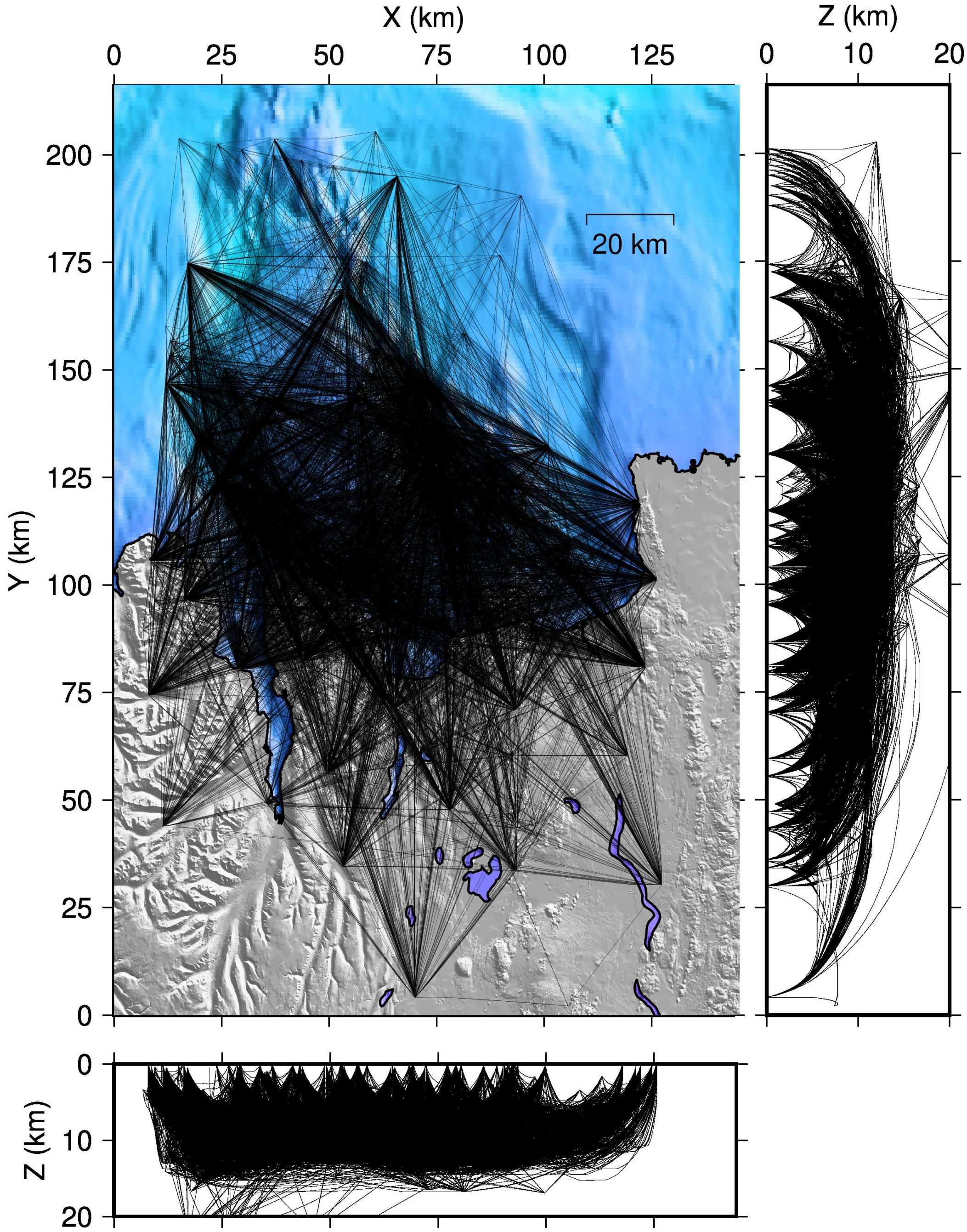

Figure 7: Ray coverage for the P- and S-waves. The map view shows good ray coverage in the center of the model, from about 75 to 150 km in the Y-direction. The lateral views show that rays are mainly subvertical in the top 3-4 km, and that ray coverage is good down to about 15 km depth.

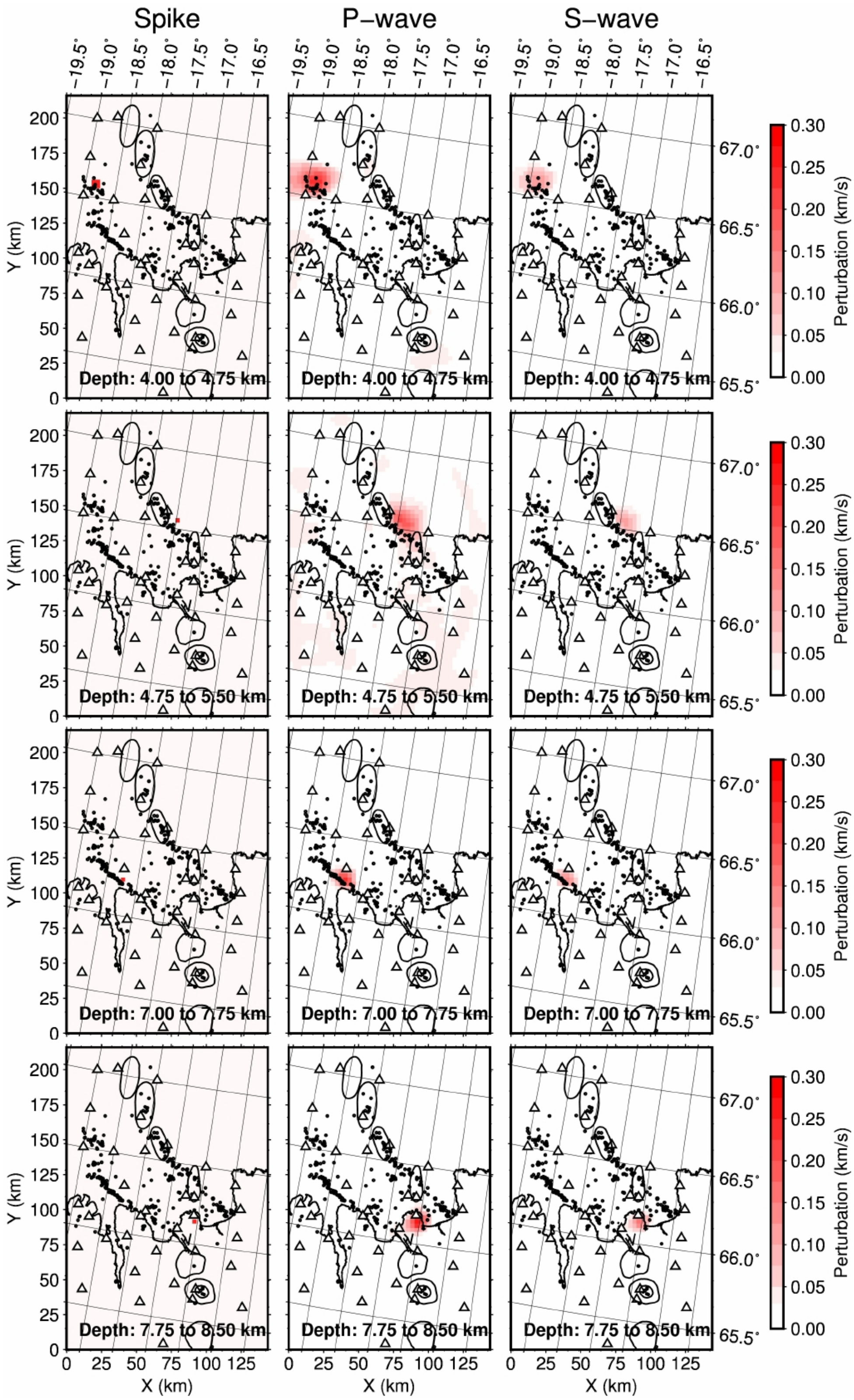

Figure 8: Spike test in the ER (top row), the GOR and the HFF (middle rows), and at the tip of the Tjörnes peninsula in between the HFF and the GOR (bottom row). Left panels show the spike perturbations added to the model. Central and right panels show the recovered P- and S-wave anomalies, respectively.

4 Results

The local earthquake tomography (LET) results include models of the distribution of P- and S-wave velocity, the Vp/Vs velocity ratio, as well as relocations of the earthquakes used. We present depth slices of the final P- and S-wave velocity models between depths of 3.25 and 8.5 km in Figure 9. Three cross-sections and their respective locations are presented in Figure 10. Two of the cross-sections (P1 and P2) are along the main lineaments, the HFF and the GOR. The third (P3) is almost perpendicular to them, crossing the HFF near Flatey Island. Cells with an accumulated length of all ray-paths crossing them of less than 8.5 km (twice the length of the cell diagonal) have been masked gray in Figures 9 and 10. The robustness of several of the main anomalies is examined by hypothesis testing described in Section 4.1. Locations of the earthquakes used in the tomography are shown as black dots in Figures 9 and 10. Only events within the depth layer (Figure 9) and within ±1 km from the sections (Figure 10) are shown. In addition to the tomographic results, we have also analyzed gravity anomalies in the study region. The derivation of the Bouguer gravity anomaly is described in Section 4.2.

The velocity structure of the study area is illuminated approximately between 3 and 15 km depth near the main lineaments (the HFF and the GOR), and the southern ER. This is also where resolution is the highest ($\sim$11 km in horizontal direction and $\sim$4 km in depth). In between the main lineaments, earthquakes are less frequent and relatively few earthquakes were recorded during the NICE experiment. Consequently, the ray path coverage is sparser there at shallow depths (see Figure 9), except in the vicinity of recording sites. The resolution length increases in general towards the periphery of the model.

The most striking feature in the velocity model at shallow depth is a low-velocity anomaly located offshore, adjacent to the main seismogenic areas of the TFZ. This anomaly appears more or less doughnut shaped at shallow depths, indented by a fast anomaly near Grímsey Island. The lowest velocities within the anomaly align on the northern side of the HFF. At 4.75-5.5 km the anomaly persist, however, at this depth it is most clearly seen on the northern side of the HFF and underneath the volcanic systems Nafir and Mánáreyar in the GOR. The low velocities along the HFF and the GOR are connected in a region extending from Flateyjarskagi Peninsula to the Mánáreyjar volcanic system. In the center of the doughnut, which coincides with Grímsey Island, velocities are high.

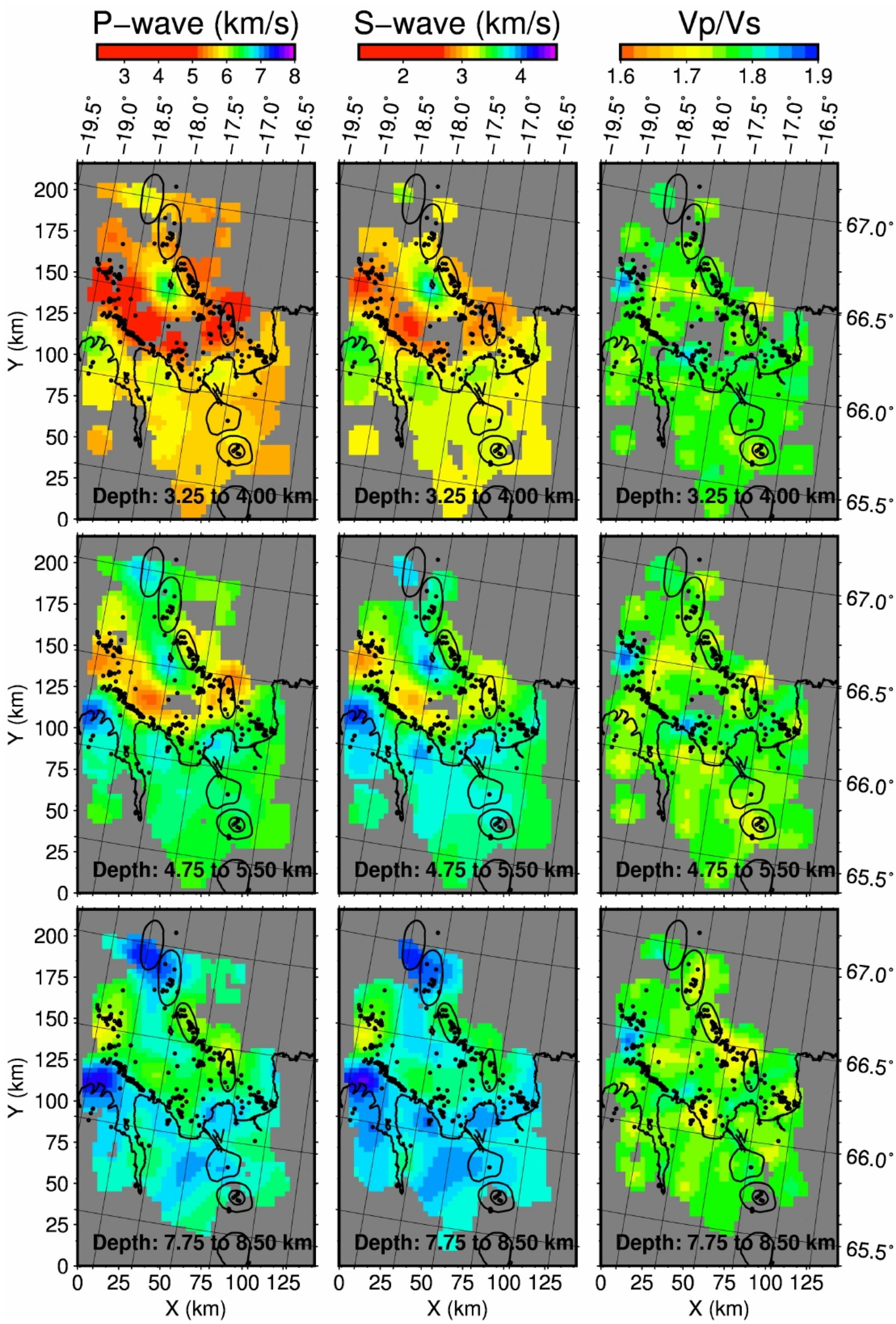

Figure 9: 3-D velocity model from the LET. The panels show map views of the model at different depth intervals. Vp and Vs velocity models are presented in the left and central panels, respectively, and the Vp/Vs ratio is shown in the right panels.

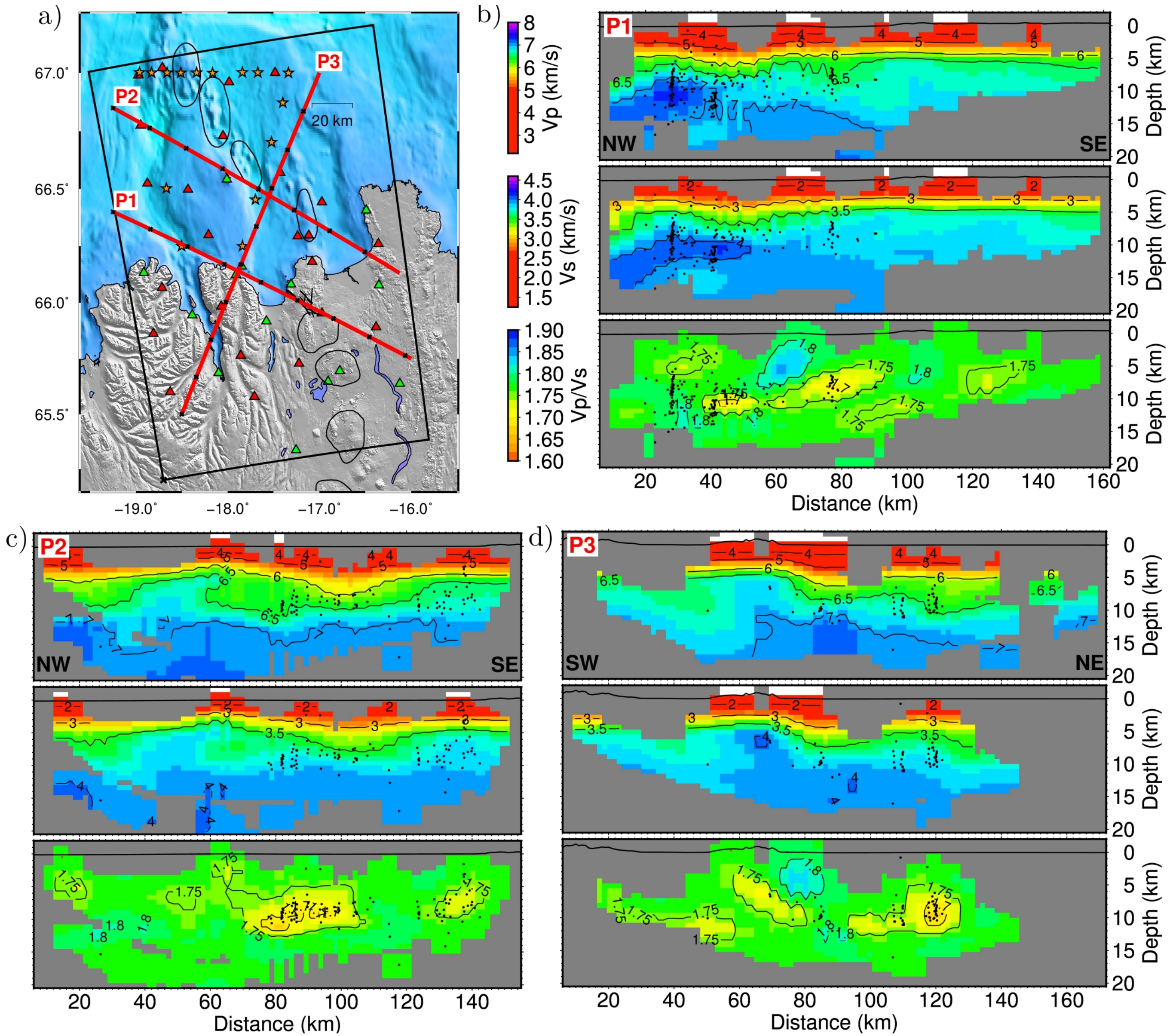

Figure 10: Cross-sections through the study area. a) Map showing the location of the cross-sections. Black crosses are set every 20 km along the lines. Cross-sections b) P1, c) P2 and d) P3 present the 3-D velocity model for P-waves, S-waves and the Vp/Vs ratio. The seismicity within ±1 km of the sections are shown as black dots.

Velocities range from above 6 km/s (P wave) and 3.5 km/s (S wave) at 3.25 km depth to nearly 7 km/s (P wave) and 4 km/s (S wave) at 5.5 km depth. At 7.75-8.5 km depth the P- and S-wave velocities are generally lower offshore than onshore. High velocities occur at this depth also in the northernmost part of the model underneath Stóragrunn. Recorded seismicity is sparse in this area and the velocity structure is primarily constrained by the explosions fired during the NICE experiment. As indicated by the ray coverage plot (Figure 7) the resolution in this area is worse than further to the south.

Localized high-velocity anomalies are present under the tips of the Tröllaskagi, Flateyjarskagi and Tjörnes Peninsulas. Of these, the anomaly beneath Tröllaskagi Peninsula is the clearest at all depths. This volume is well resolved despite its location near the border of the study area due to the two stations located there, one permanent station of the SIL network (sig) and one temporary station, and the abundant seismicity in the ER. The smallest of the named features are nominally resolved according to our model appraisal and resolution analysis. The larger anomalies are clearly resolved. Correlated low velocities for P and S waves were also reported by *Riedel et al.* [2005] along the HFF at 7 to 12 km depth, although their resolution is not clearly demonstrated. They also report a NS trending, elongate, low-velocity feature at 7 km depth north of Skjálfandi Bay. Its linear shape is not clear in P-wave velocities and this feature likely corresponds to the low-velocity link we map between Flateyjarskagi and the Mánáreyjar Volcanic System.

The data do not require dramatic variations of the Vp/Vs ratio as shown in Figures 9 and 10. The clearest low Vp/Vs anomaly is located near the northern end of the Mánáreyjar volcanic system east of Grímsey Island. It is localized near the surface and spreads along the GOR to the northwest with increasing depth (e.g. at 7.75-8.5 km depth in Fig. 9). The Vp/Vs ratio is close to 1.7. Another low Vp/Vs anomaly of similar amplitude is found at 7.75-8.5 km depth SE of Flatey Island. The most prominent positive Vp/Vs anomaly is located in the southern part of Eyjafjarðaráll Basin, where Vp/Vs is $\sim$1.85. A smaller positive Vp/Vs anomaly is found along the HFF beneath Flatey Island.

Several of the same features are highlighted in the cross-sections in Figure 10, which also extend to greater depth than the depth slices in Figure 9 show. In profile P1 (along the HFF), the prominent low-velocity anomaly along the HFF is clearly seen at distances between 40 and 80 km as suppressed iso-velocity contours, though this anomaly is centered just north of the HFF and not underneath the profile. The low Vp/Vs ratio observed at depth near Flatey Island extends and deepens to the NNW underneath the HFF between 40 and 100 km. East of there, the profile lies on land and crosses the Northern Volcanic Zone of Iceland. In that part the structure appears quite homogeneous, with the P-wave 6.5 km/s iso-velocity contour at approximately 5 km depth. At the western end the structure along profile P1 is different. Here, the upper crust (depth to the Vp=6.5 km/s iso-velocity contour) is similar to the eastern end, but very high velocities, above 7 km/s, reach above 10 km depth. This part of the profile crosses the high-velocity anomaly near the northern tip of Tröllaskagi Peninsula, which spreads over a larger area at depth. The velocities reach a slightly higher value further south.

The high Vp/Vs anomaly at Flatey Island appears at 2 to 5 km depth. Profile P2 lies along the GOR east of Grímsey Island in its eastern half and crosses the northern part of the Grímsey Shoal and the northern part of Eyjafjarðaráll Rift to the WNW. At a distance of about 100 km, near the Mánáreyjar volcanic system, the depth to the Vp=6 km/s iso-velocity contour is depressed. The interior of the Grímsey Shoal appears as a high-velocity anomaly at distances between 40 and 60 km. A low Vp/Vs anomaly spreads out along the GOR between the Nafir and Mánáreyjar volcanic systems at 6-12 km depth. A small Vp/Vs low is found near the eastern end of profile P2 where the GOR connects with the Krafla Fissure Swarm. Profile P3 lies transverse to the main lineaments of the TFZ past Flatey Island. It crosses the HFF and profile P1 at about 75 km distance and the GOR and profile P2 at about 110 km. On land, beneath the southernmost third of the profile, the structure is rather homogeneous and similar to the SE end of profile P1 with the P-wave 6.5 km/s iso-velocity contour at about 5 km depth. A sharp change in structure occurs where the profile crosses the HFF close to Flatey Island at about 75 km. Offshore, the depth to the P-wave 6.5 km/s iso-velocity contour is close to 10 km. Just south of the HFF, relatively high velocities reach the near surface. This is a small high-velocity anomaly beneath the Flateyjarskagi Peninsula. A band of low Vp/Vs arcs along the profile at depth. This is clearest at 120 km distance just north of the GOR. This is the anomaly earlier associated with the area in between the Mánáreyjar and Nafir volcanic centers.

4.1 Hypothesis Test

The spike tests described in section 3.4.1 address the issue of resolution in the tomography in a general sense. Estimating resolution in LET is difficult task because the locations of both the ray paths and the earthquakes are controlled by the specifics of the velocity models. These effects can be particularly strong in a velocity model with strong small-scale velocity heterogeneity. Our results contain 20% velocity variations in the shallow parts of the model causing both strong lateral and vertical velocity gradients. In order to analyse the robustness of some specific model features, we conducted a series of hypothesis tests.

For these tests, the selected anomalies were removed from the final velocity model by replacing them with a regional velocity average. This model was then used as a starting model for a few more inversion. This procedure allows the inversion to recover the anomaly in the velocity model if it is required by the data. We present tests of three anomalous regions, two regions within the doughnut shaped shallow velocity anomaly offshore, and the high-velocity anomaly beneath Tröllaskagi.

The results are presented in Figure 11. The left panels show the initial P-wave velocity model with a specific anomaly removed from the model. The right panels show the recovered velocity model after inversion. The three tested anomalies are all recovered in shape and amplitude, albeit not in detail. This indicates that the tested anomalies are required by data and are not strongly affected by the specific non-linear effects of the model, giving us confidence to interpret them as realistic features of the crustal structure in the TFZ.

4.2 Bouguer gravity anomaly

Variations on the crustal velocities can be associated with variations on the density of rocks. A clear gravity low located offshore the Tjörnes Fracture Zone has been reported in the compilation of free-air gravity anomaly by *Eysteinsson and Gunnarsson* [1995]. That motivated us to estimate the Bouguer gravity in the area and compare it with our tomographic results. To estimate the Bouguer-gravity anomaly, we used the free-air gravity data from *Sandwell and Smith* [2009] and *Sandwell et al.* [2013, 2014], determined at an altitude of 0 m. Those data were smoothed with a filter of 14 km wavelength [*Sandwell et al.*, 2013], and have a resolution of 7 km. The free-air gravity anomaly is overprinted by variations in the topography. Therefore, we corrected it for topographic effects [*Forsberg*, 2003] applying a Bouguer-plate correction and a terrain correction, using elevation data from *Smith and Sandwell* [1997]. The smoothing filter applied to the free-air gravity anomaly was also applied to the elevation data to reduce the contribution of small-scale

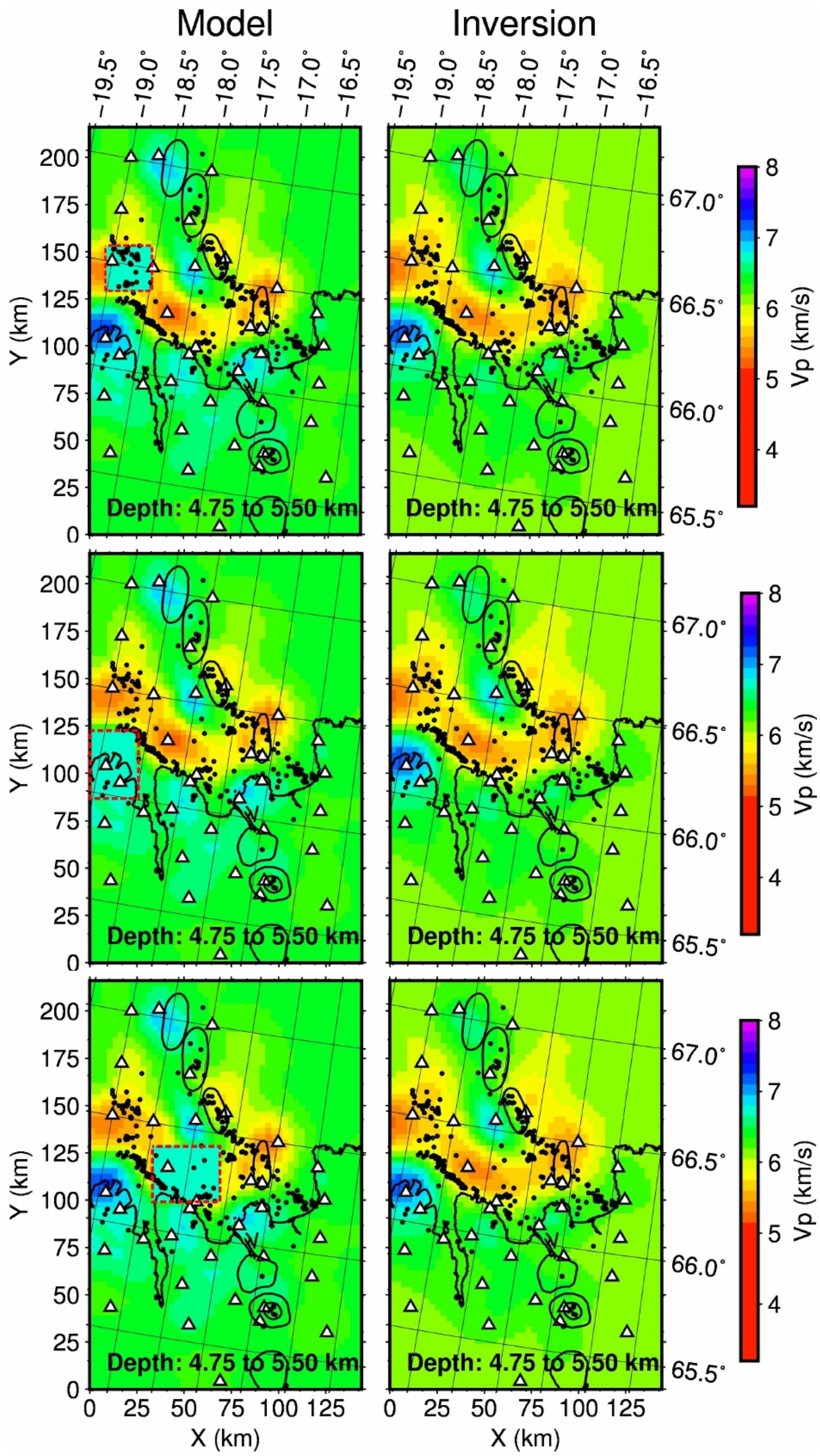

Figure 11: Hypothesis tests removing low-velocity anomalies in the ER and the central HFF, and a high-velocity anomaly beneath Tröllaskagi Peninsula. Left panels show the starting velocity model with the anomaly removed. Red dashed rectangle encloses the removed anomaly. Right panels show the recovered velocity model after reinversion.

anomalies in the Bouguer anomaly. We present the Bouguer-gravity anomaly after the described processing in Figure 12 (a) and the detrended anomaly in Figure 12 (b). In the detrending we have removed the best fitting North/South dipping plane. The removed trend likely includes effects of crustal thinning towards the north and the transition from Icelandic to a more oceanic crust.

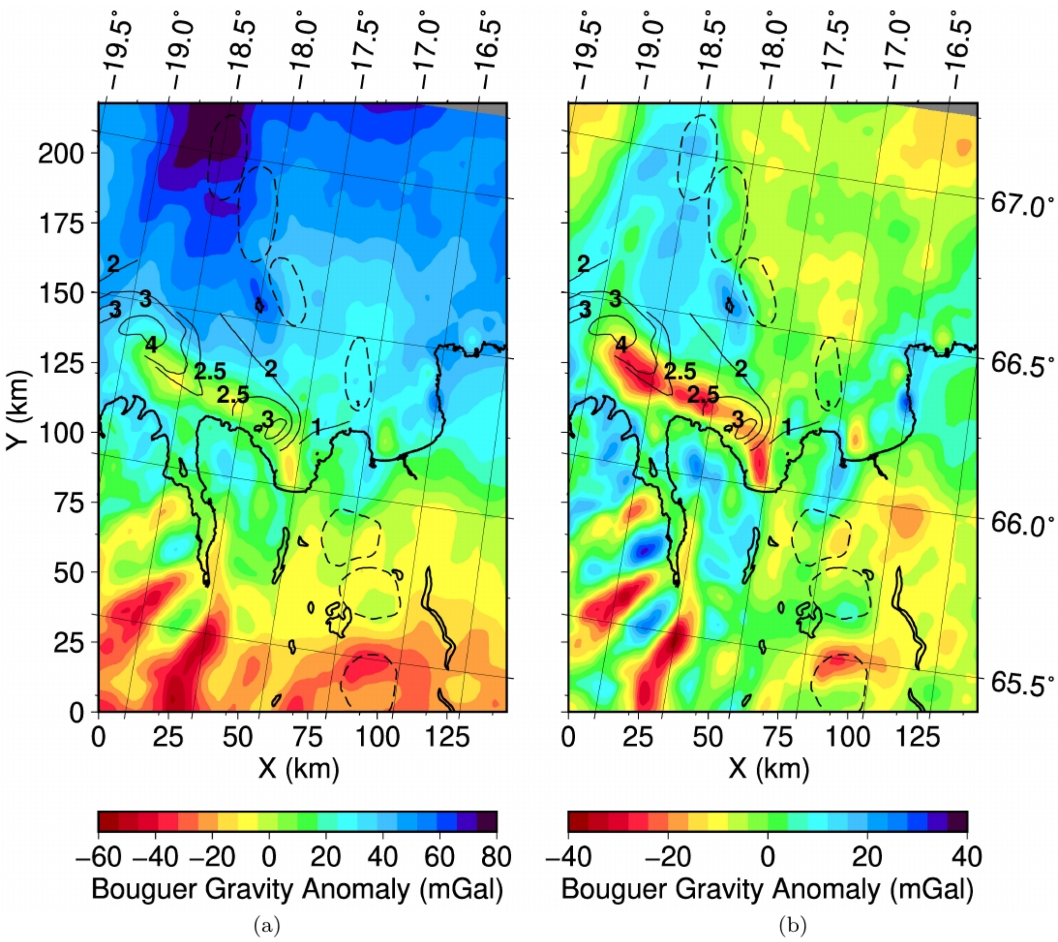

Figure 12: Bouguer gravity anomaly based on *Sandwell and Smith* [2009] and *Sandwell et al.* [2013, 2014], and contour lines of sediment thickness estimated by *Gunnarsson* [1998] (see also *Richter and Gunnarsson* [2010]). The maps present (a) the Bouguer anomaly and (b) the detrended Bouguer anomaly removing the best fitting, northward, linear trend.

The detrended Bouguer anomaly shows a curvilinear feature along the HFF with an axis parallel to and just north of the HFF. It is 10-15 km wide and its amplitude reaches about -40 mGal. Its orientation swings toward the north at the ER and toward the south in Skjálfandi Bay. Additionally, increased gravity values can be found along the axis of the

ER ($\sim$ 10 mGal) and at Grímsey Island ($\sim$ 20 mGal), while a gravity low is located north of the Tjörnes Peninsula (just north of 66.5^o).

Up to 4 km thick sediments from the Quaternary [*Eiríksson et al.*, 2000; *Søndergaard*, 2010; *Gudmundóttir*, 2010] and Holocene [*Solomina et al.*, 2015] periods have been mapped in our study region by *Gunnarsson* [1998] and *Richter and Gunnarsson* [2010], and are represented as thickness contours in Figure 12. The sediments are thickest along and north of the HFF, but the negative gravity anomaly is not strongest where the sediments are mapped thickest, and the sediment anomaly extends in a broader area than the gravity anomaly. Of course, the gravity integrates density structures to depth and may at the longer wavelengths contain signature of deeper structures, e.g., crustal thickness variations.

5 Discussion

One of the more prominent feature in the velocity model is the linear band of low velocities along the northern side of the offshore part of the HFF. This anomaly is about 60 km long, 20 km wide and extends from the southern part of the ER to Skjálfandi Bay. It reaches 5.5 km depth and is well resolved according to the spike and hypothesis tests. Small variations of the Vp/Vs ratio are associated with this anomaly, most notably a small high at Flatey Island, strongest at about 5 km depth. A broader and deeper low Vp/Vs anomaly that is strongest just east of Flatey Island near the ESE end of the anomaly, extends along the fault zone at depth and deepens to the NW (see Figure 10 (b)).

The HFF low velocity anomaly is co-located with a gravity low along the northern side of the HFF (Figure 12). The width of the HFF gravity low suggests that the bulk of its density sources lie above about 5 km depth. If so, its amplitude can be explained with a density contrast up to 500 kg/m^3. This can be a reasonable contrast between Quaternary sediments and volcanic upper-crustal rocks, although the uppermost crust in Iceland is quite porous and characterized by low seismic velocities and relatively low density [*Pálmason*, 1971]. Thus, the crude features of the gravity anomaly could be explained by the sediments though the along-strike variations of the sediment thickness do not coincide in detail with the variations within the gravity anomaly. As the low velocities continue into the ER, this would require invoking a deeper density high underneath the western end of the sediment distribution. Tentatively, the source of the broad gravity high along the ER may thus continue further to the south and be associated with the high velocities observed under the NW end of Profile 1 (Figure 10 (b)). Perhaps the crust is thinner beneath the ER due to its avolcanic rifting. It should be noted that sediments compact with pressure at depth and 500 kg/m^3 may therefore be a large value for an average over about 5 km. The sediment distribution is generally too broad to explain the narrow gravity anomaly. Also, the velocity anomaly reaches depths that exceed the sediment thickness spread by the finite depth resolution of the tomography ($\sim$3 km). Therefore, we conclude that a part of the low velocities along the north side of the HFF are likely due to the sediments, but the anomaly at depth cannot only be due to smearing of the signature of the sediments to depth. Also, shallow, fresh sediments are expected to posses a high Vp/Vs ratio [*Kondilarov et al.*, 2015]. No such systematic anomaly is seen in the tomographic results, only a small, localized, positive anomaly at Flatey Island concentrated at 5 km depth and another in the southern ER.

At greater depth, low velocities are associated with the HFF and GOR (as well as in between them north of Skjálfandi and Tjörnes) to approximately 10 km depth. Similar deep low velocities have been mapped at other oceanic transforms [*Avendonk et al.*, 2001; *Roland et al.*, 2012]. This may be caused by fracturing of the crustal rocks due to the shearing deformation around the transform or excess hydrous alteration due to water percolating through the fractures from above. If so, one would expect associated density anomalies at depth, which, in turn, would contribute to the broader features of the Bouguer anomalies in Figure 12. Serpentinization of the mantle beneath the fracture zone and subsequent ascent of light serpentinite into the crust [*Hensen et al.*, 2019] is possible given the high density of the lower crust in Iceland [*Gudmundsson*, 2003], but seems unlikely because of the thickness of the crust (15-20 km [*Darbyshire et al.*, 2000]) as such deep fractures may not be significantly permeable.

Low Vp/Vs ratios are mapped at 5-10 km depth beneath much of the HFF, dipping gently to the WNW (see Figure 10, profile P1). They are not present on land at the ESE end of the profile, where the crustal structure is relatively homogeneous and similar to average Icelandic crust [*Pálmason*, 1971; *Flóvenz*, 1980], or at the WNW end of the profile, where the HFF merges with the ER. Fractured rock, saturated with highly compressible fluid, will have a low Vp/Vs ratio [*Tryggvason et al.*, 2002; *Wang et al.*, 2012]. Therefore, these anomalies may indicate the presence of supercritical H_2O or other compressible fluid. The critical point of water is at approximately 375^{o}C. If this condition is reached at 5 km depth, that would imply a temperature gradient of 75^{o}C/km, which is feasible in the Icelandic crust [*Flóvenz and Sæmundsson*, 1993].

The part of the doughnut shaped low-velocity anomaly in the top 5.5 km of the crust that is located along the HFF is discussed previously. The anomaly extends from the HFF near Flatey Island to the NE and into the GOR and the Mánáreyjar volcanic system (Figure 9). Low velocities also extend along the GOR towards the NW. The low-velocity anomaly appears to reach the greatest depth near the Nafir and Mánáreyjar volcanic systems (Figure 10 (d)). This pattern of low-velocity anomalies resembles the distribution of weak gravity lows ($\sim$ 10 mGal) in the gravity maps in Figure 12 (b), although the gravity anomaly extends further north beyond the well-resolved part of the velocity model. Relatively thin sediments are found in this region [*Sturkell et al.*, 1992; *Gunnarsson*, 1998; *Richter and Gunnarsson*, 2010] and no clear sediment thickness anomalies are mapped, but information is sparse. This part of the low-velocity anomaly coincides with the strongest low Vp/Vs anomaly in our results, visible along profile P2 at 75-100 km between the Nafir and Mánáreyjar volcanic systems at 5 and 10 km depth (Figure 10 (c)). Its interpretation is not obvious. We speculate that along the GOR the low velocities may relate to the volcanism of the area, and argue that the similarity of the gravity anomaly to the velocity anomaly lends the latter support. The low Vp/Vs ratios may indicate the presence of supercritical fluids within the volcanic systems.

The eye of the doughnut, the high velocities around Grímsey Island, clearly coincide with a local gravity high ($\sim$30 mGal) corroborating the tomographic result. This anomaly appears along profile P2 in Figure 10 at distances between 40 and 60 km as an updoming of the the 6.5 km P-wave iso-velocity contour. Grímsey Island sits on the Grímsey Shoal comprising the western half of the Tjörnes Microplate which is devoid of seismicity in the SIL catalog. One possible explanation of this anomaly is in terms of shallow cumulates associated with an extinct Tertiary volcanic center, possibly from an earlier configuration of spreading. We also note that about half of the crustal accretion history of Iceland since the reconfiguration of spreading from the Ægir Ridge to the Kolbeinsey Ridge about 30 million years ago is apparently missing in the surface geology of Iceland [*Foulger*, 2006], due to ridge jumps and the aerial extent of basaltic volcanism. Therefore, blocks of older crust (15 - 30 million years old) are hidden underneath younger lava flows. *Foulger* [2006] argued that this may complicate the distribution of crustal thickness in Iceland and possibly explain low-velocity zones in the middle of the crust ($\sim$10 km depth) as light differentiated components (e.g. felsic rocks) concentrated near the surface of these blocks may be buried to significant depth. Likewise, if such a block was heavily eroded, it could explain high mid-crustal velocities in the near surface such as those mapped beneath the Grímsey Shoal.

The high velocities beneath the northern tip of Tröllaskagi Peninsula exceed a P-wave velocity of 7 km/s at 5 km depth. This high velocity is difficult to explain at such shallow depth. It is similar to velocities found in the lower crust likely to consist of compressed crystalline intrusives and cumulates possibly with higher olivine content than normal Icelandic crust [*Gudmundsson*, 2003]. Spike and hypothesis testing indicates that this anomaly is well resolved. It is not associated with anomalous Vp/Vs estimates. Some rhyolite is found exposed in the area according to the geological map of *Jóhannesson* [2014]. Therefore, we suggest that this anomaly may relate to a poorly exposed Tertiary volcanic center, i.e. it cumulates beneath a relic shallow magma reservoir similar to the one mapped by *Brandsdóttir et al.* [1997] beneath Krafla volcano and by *Jeddi et al.* [2017] at Katla. Similar, but less pronounced high-velocity anomalies underneath the Flateyjarskagi and Tjörnes Peninsulas may have the same explanation. Some correlation with local gravity highs (10-20 mGal) is found in these areas.

High velocities at depth (5-10 km) beneath the NW end of the GOR also coincide with a gravity high which extends to the south along the ER. This may be caused by crustal thinning in the melt starved rift and it is possible that our first-arrival-time tomography is affected by mantle waves (Pn, Sn) although we have not been able to identify any PmP (or SmS) phases to constrain the crustal thickness.

6 Conclusions

A 3-D velocity model for the TFZ has been estimated by LET, using data from the NICE experiment carried out during the summer of 2004. Several velocity anomalies have been identified in the velocity model, which relate to the tectonic elements of this complex transform region.

- The HFF is for much of its length (from its western end to Flatey Island) delineated by a low-velocity anomaly on its northern side that extends to at least 5.5 km depth. A curvilinear Bouguer gravity low coincides with this anomaly, although the gravity anomaly is considerably narrower. Anomalously thick (up to 4 km) Quaternary sediments are found in the same general area. Velocities remain low at greater depth as a part of a larger region in between and including the GOR. We interpret the deeper parts of this velocity anomaly beneath the ESZ as due to fracturing of rocks at depth due to the stress field and motion of this transform segment of the TFZ.

- A band of low Vp/Vs anomalies is found along the same segment of the HFF at a depth of 5-10 km. We interpret this feature as due to supercritical fluids in the deep fractures of the segment.
- Low velocities are also found along the volcanic northwestern part of the GOR that may relate to anomalous temperatures in the upper crust, e.g., due to intrusion, or fracturing of the crust. Low Vp/Vs is also mapped in this region at depth and may again be caused by supercritical fluids (melt is too incompressible to cause a low Vp/Vs ratio).
- The northern part of the Grímsey Shoal appears as a fast anomaly in the upper crust. This may be the signature of a relic Tertiary (Miocene/Pliocene) volcano or an older (Oligocene/early Miocene) eroded crustal block.
- Upper crustal velocities are higher on land than at sea. In particular, localized high-velocity anomalies are mapped beneath the Tröllaskagi and Flateyjarskagi Peninsulas. These may be the signatures of relic Tertiary volcanic centers with which exposed rhyolites are associated.

Acknowledgments

We thank the NICE project and its participants for allowing us to use the recorded data during the experiment. The fieldwork and logistics for the temporary seismic land stations were supported by the Swedish Research Foundation, grant 2003-3600. The acquisition of Ocean Bottom data was supported by the German Research Foundation (DFG) under projects Da478/13-1 and RI1220/2-1 and the University of Hamburg. We thank Ragnar Stefánsson, Kristján Tryggvason, Carsten Riedel, Martin Hensch and Tryggvi Pálsson, who helped out during the fieldwork. Moreover, we are grateful to the Icelandic Meteorological Office - IMO for providing us the waveforms of earthquakes recorded by the SIL network in North Iceland during the time of the NICE project. Finally, we thank the ChEESE project and its principal researcher at IMO, Benedikt Halldórsson, for supporting

the revision of this document in its final stage. Datasets for this research are available in *Abril et al.* [2020].

References

Abril, C., O. Gudmundsson, and the SIL seismological group (2018), Relocating earthquakes with empirical traveltimes, *Geophys. J. Int.*, *214(3)*, 2098–2114.

Abril, C., A. Tryggvason, O. Gudmundsson, and R. Steffen (2020), Database of earthquake locations (summer 2004), Bouguer gravity anomaly, and P- and S-wave 3-D velocity models of the Tjörnes Fracture Zone (North Iceland), `https://uppsala.app.box.com/s/3df9bye08dd0w3keyyksrwycl1dn1li7`, [Online; accessed 6-June-2020].

Aster, R., B. Borchers, and C. Thurber (2005), *Parameter estimation and inverse problems. International Geophysics Series 90 (ed. R. Domowska, J.R. Holton and H.T. Rossby)*, Elsevier Academic Press, Burlington.

Avendonk, H., A. Harding, and J. Orcutt (2001), Contrast in crustal structure across the Clipperton transform fault from travel time tomography, *J. Geophys. Res.*, *106(B11)*, 10,961–10,981.

Bodvarsson, R., S. Rognvaldsson, S. Jakobsdottir, R. Slunga, and R. Stefansson (1996), The SIL data acquisition and monitoring system, *Seismol. Res. Lett.*, *67(5)*, 35–46.

Bödvarsson, R., S. Rögnvaldsson, R. Slunga, and E. Kjartansson (1999), The SIL data acquisition system - at present and beyond year 2000, *Phys. Earth Planet. Inter.*, *113(1-4)*, 89–101.

Brandsdóttir, B., W. Menke, P. Einarsson, and R. White (1997), Färoe-Iceland Ridge Experiment 2. Crustal structure of the Krafla central volcano, *J. Geophys. Res.*, *102(B4)*, 7867–7886.

Darbyshire, F., K. Priestley, R. White, R. Stefánsson, G. Gudmundsson, and S. Jakobsdóttir (2000), Crustal structure of central and northern Iceland from analysis of teleseismic receiver functions, *Geophys. J. Int.*, *143*, 163–184.

Einarsson, P. (2008), Plate boundaries, rifts and transforms in Iceland, *Jökull*, *58*, 35–58.

Eiríksson, J., K. Knudsen, H. Haflidason, and P. Henriksen (2000), Late-glacial and Holocene paleoceanography of the North Icelandic Shelf, *J. of Quaternary Science*, *15(1)*, 23–42.

Eysteinsson, H., and K. Gunnarsson (1995), Maps of gravity, bathymetry and magnetics for Iceland and surroundings, Report OS-95055/JHD-07, National Energy Authority, Reykjavik, Iceland.

Flóvenz, Ó. (1980), Seismic structure of the Icelandic crust above layer three and the relation between body wave velocity and the alteration of the basaltic crust, *J. Geophys.*, *47(1-3)*, 211–220.

Flóvenz, O., and K. Sæmundsson (1993), Heat flow and geothermal processes in Iceland, *Tectonophys.*, *225*, 123–138.

Forsberg, R. (2003), An overview manual for the GRAVSOFT Geodetic Gravity Field Modelling Programs, National Survey and Cadastre of Denmark.

Foulger, G. (2006), Older crust underlies Iceland, *Geophys. J. Int.*, *165*, 672–676.

Gudmundóttir, E. (2010), Tephra stratigraphy and land-sea correlations: A tephrochronological framework based on marine sediment cores off North Iceland, Ph.D. thesis, Faculty of Earth Sciences, University of Iceland.

Gudmundsson, O. (2003), The dense root of the Iceland crust, *Earth. Planet. Sci. Lett.*, *206*, 427–440.

Gunnarsson, K. (1998), Sedimentary basins of the N-Iceland shelf, Report OS-98014, National Energy Authority, Reykjavik, Iceland.

Havskov, J., and L. Ottemöller (1999), SEISAN Earthquake analysis software, *Seis. Res. Lett.*, *70*, 532–534.

Hensch, M., C. Riedel, J. Reinhardt, T. Dahm, and T. NICE-People (2008), Hypocenter migration of fluid-induced earthquake swarms in the Tjörnes Fracture Zone, *Tectonophys.*, *447*, 80–94.

Hensch, M., G. Guðmundsson, and the SIL monitoring group (2013), Offshore seismicity with large azimuthal gaps: Challenges for the SIL network, in *Proceedings of the International Workshop on Earthquakes in North Iceland*, Húsavík, Iceland.

Hensen, C., J. Duarte, P. Vannucchi, A. Mazzini, M. Lever, P. Terrinha, L. Géli, P. Henry, H. Villinger, J. Morgan, M. Schmidt, M.-A. Gutscher, R. Bartolome, Y. Tomonaga, A. Polonia, E. Gràcia, U. Tinivella, M. Lupi, M. Çağatay, M. Elvert, D. Sakellariou, L. Matias, R. Kipfer, A. Karageorgis, L. Ruffine, V. Liebetrau, C. Pierre, C. Schmidt, L. Batista, L. Gasperini, E. Burwicz, M. Neres, and M. Nuzzo (2019), Marine Transform Faults and Fracture Zones: A joint perspective integrating seismicity, fluid flow and life, *Front. Earth Sci.*, *7(39)*, 1–29.

Hole, J. (1992), Nonlinear high-resolution three-dimensional seismic travel time tomography, *J. Geophys. Res*, *97(B5)*, 6553–6562.

Jeddi, Z., O. Gudmundsson, and A. Tryggvason (2017), Ambient-noise tomography of Katla volcano, south Iceland, *J. Volcanol. Geoth. Res.*, *347*, 264–277.

Jóhannesson, H. (2014), Geological Map of Iceland – Bedrock geology – 1:600000, The Icelandic Institute of Natural History, Reykjavik, Iceland.

Kodaira, S., R. Mjelde, K. Gunnarsson, M. Shiobara, and H. Shimamura (1997), Crustal structure of the Kolbeinsey Ridge, North Atlantic, obtained by use of ocean bottom seismographs, *J. Geophys. Res.*, *102 B2*, 3131–3151.

Kondilarov, A., R. Mjelde, E. Flueh, and R. Pedersen (2015), Vp/Vs ratios and anisotropy on the northern Jan Mayen Ridge, North Atlantic, determined from ocean bottom seismic data, *Polar Science*, *9*, 293–310.

Magnúsdóttir, S., B. Brandsdóttir, N. Driscoll, and R. Detrick (2015), Postglacial tectonic activity within the Skjálfandadjúp Basin, Tjörnes Fracture Zone, offshore Northern Iceland, based on high resolution seismic stratigraphy, *Mar. Geol.*, *367*, 159–170.

Menke, W., M. West, B. Brandsdóttir, and D. Sparks (1998), Compresseional and shear velocity structure of the lithosphere in northern Iceland, *Bull. Seis. Soc. Am.*, *88*, 1561–1571.

Paige, C., and M. Saunders (1982), LSQR: An algorithm for sparse linear equations and sparse least squares, *ACM Transactions on Mathematical Software*, *8*, 43–71.

Pálmason, G. (1971), Crustal structure of Iceland from explosion seismology, PhD thesis.

Pavlis, G., and J. Booker (1980), The mixed discrete-continuous inverse problem: Application to the simultaneous determination of earthquake hypocenters and velocity structure, *J. Geophys. Res.*, *85(B9)*, 4801–4810.

Podvin, P., and I. Lecomte (1991), Finite difference computation of traveltimes in very contrasted velocity models: a massively parallel approach and its associated tools, *Geophys. J. Int.*, *105*, 271–284.

Richter, B., and K. Gunnarsson (2010), Overview of hydrocarbon related research in Tjönes, Report Project No. 503402, National Energy Authority, Reykjavik, Iceland.

Riedel, C., A. Tryggvason, T. Dahm, R. Stefanson, R. Bodvarson, and G. Gudmundsson (2005), The seismic velocity structure north of Iceland from joint inversion of local earthquake data, *J. Seis.*, *9*, 383–404.

Riedel, C., A. Tryggvason, B. Brandsdottír, T. Dahm, R. Stéfansson, M. Hensch, R. Bödvarsson, K. Vogfjord, S. Jakobsdottír, T. Eken, R. Herber, J. Holmjarn, M. Schnese, M. Thölen, B. Hofmann, B. Sigurdsson, and S. Winter (2006), First results from the

North Iceland experiment, *Mar. Geophys. Res.*, *27*, 267–281.

Rögnvaldsson, S., A. Gudmundsson, and R. Slunga (1998), Seismotectonic analysis of the Tjörnes Fracture Zone, an active transform fault in north Iceland, *J. Geophys. Res.*, *103*, 117–129.

Roland, E., D. Lizzarralde, J. McGuire, and J. Collins (2012), Seismic velocity constraints on the material properties that control earthquake behavior at the Quebrada-Discovery-Gofar transform faults, East Pacific Rise, *J. Geophys. Res.*, *117(B11102)*, 10,961–10,981.

Sæmundsson, K. (1973), Evolution of the axial rifting zone in Northern Iceland and the Tjornes Fracture Zone, Report OSJHD7303, National Energy Authority, Reykjavik, Iceland.

Sandwell, D., E. Garcia, K. Soofi, , P. Wessel, M. Chandler, and W. Smith (2013), Toward 1-mGal accuracy in global marine gravity from CryoSat-2, Envisat, and Jason-1, *The Leading Edge*, *32(8)*, 892–899, doi:10.1190/tle32080892.1.

Sandwell, D. T., and W. H. F. Smith (2009), Global marine gravity from retracked Geosat and ERS-1 altimetry: Ridge Segmentation versus spreading rate, *J. Geophys. Res.*, *114*, B01,411, doi:10.1029/2008JB006008.

Sandwell, D. T., R. D. Müller, W. H. F. Smith, E. Garcia, and R. Francis (2014), New global marine gravity model from CryoSat-2 and Jason-1 reveals buried tectonic structure, *Science*, *346*, 65–67, doi:10.1126/science.1258213.

Smith, W. H. F., and D. T. Sandwell (1997), Global seafloor topography from satellite altimetry and ship depth soundings, *Science*, *277*, 1957–1962, doi:10.1126/science.277.5334.1956.

Solomina, O., R. Bradley, D. Hodgson, S. Ivy-Ochs, V. Jomelli, A. Mackintosh, A. Nesje, L. Owen, H. Wanner, G. Wiles, and N. Young (2015), Holocene glacier fluctuations, *Quaternary Science Reviews*, *111*, 9–34.

Søndergaard, M. (2010), Lateglacial and holocene paleoclimatic fluctuations of the North Icelandic shelf - Foraminiferal analysis, sedimentology and tephrochronology of Core MD99-2275, Ph.D. thesis, Department of Earth Sciences, University of Aarhus.

Stefansson, R. (1979), Catastrophic earthquakes in Iceland, *Tectonophys.*, *53(3-4)*, 273–278.

Sturkell, E., B. Brandsdóttir, H. Shimamura, and M. Mochizuki (1992), Seismic crustal structure along the Axarfjörður trough at the eastern margin of the Tjörnes Fracture

Zone, N-Iceland, *Jökull*, *42*, 13–23.

Tryggvason, A. (1998), Seismic tomography: Inversion for P- and S-wave velocities, Ph.D. thesis, Uppsala University.

Tryggvason, A., and B. Bergman (2006), A travel time discrepancy in the Podvin & Lecomte *time3d* finite difference algorithm, *Geophys. J. Int.*, *165*, 432–435.

Tryggvason, A., S. Rögnvaldsson, and O. Flóvenz (2002), Three-dimensional imaging of the P- and S-wave velocity structure and earthquake locations beneath Southwest Iceland, *Geophys. J. Int.*, *151*, 848–866.

Wang, X., A. Schubnel, J. Fortin, E. David, Y. Gueguen, and H. Ge (2012), High Vp/Vs ratio: Saturated cracks or anisotropic effects?, *Geophys. Res. Lett.*, *39*, L11,307.

Figure 1.

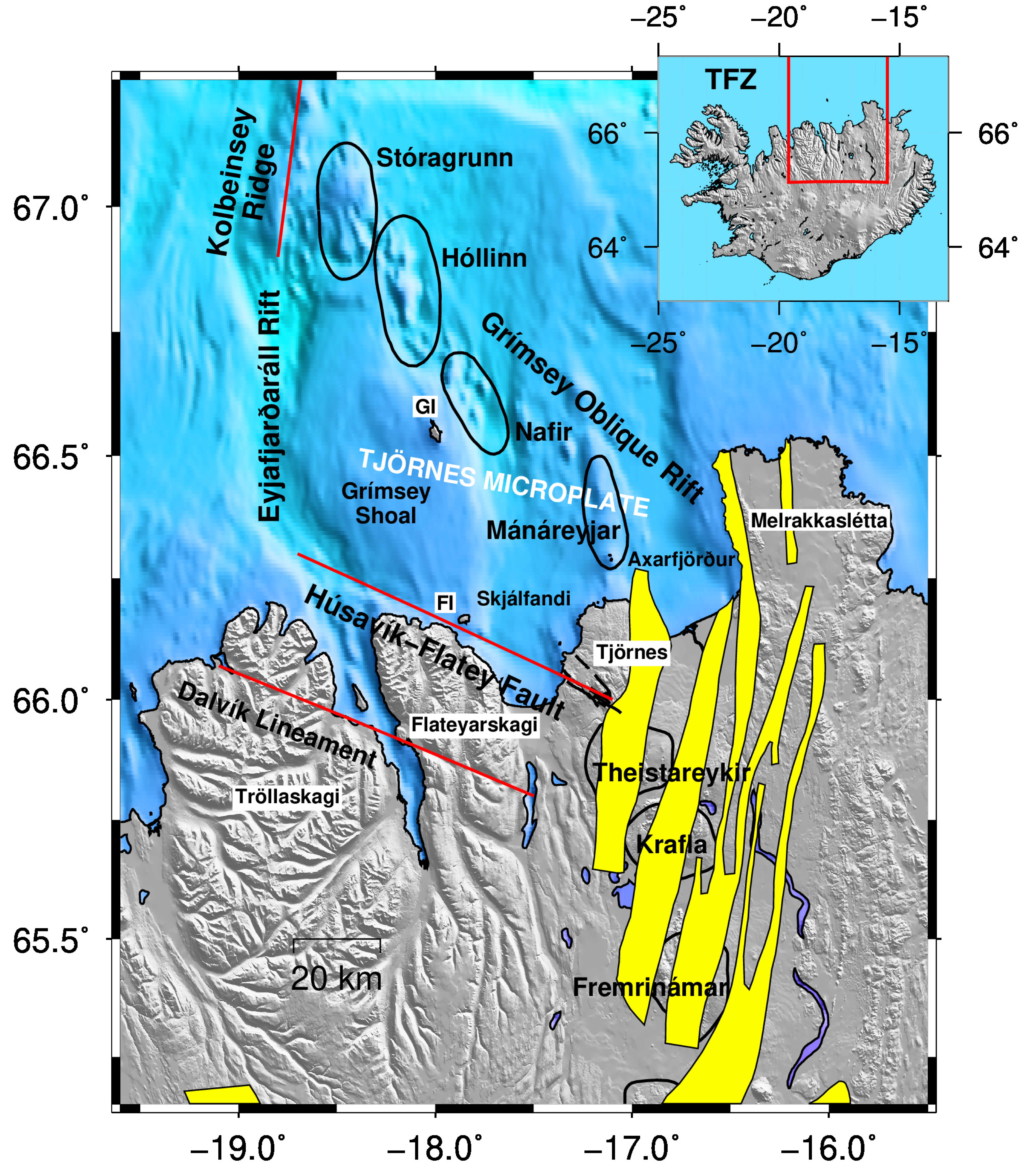

TFZ
–25˚
–20˚
–15˚
66˚
64˚
Kolbeinsey Ridge
Stóragrunn
Hóllinn
Eyjafjarðaráll Rift
Grímsey Oblique Rift
GI
Nafir
TJÖRNES MICROPLATE
Grímsey Shoal
Mánáreyjar
Melrakkaslétta
Axarfjörður
FI
Skjálfandi
Húsavík–Flatey Fault
Tjörnes
Dalvík Lineament
Flateyarskagi
Theistareykir
Tröllaskagi
Krafla
20 km
Fremrinámar
67.0˚
66.5˚
66.0˚
65.5˚
–19.0˚
–18.0˚
–17.0˚
–16.0˚

Figure 2.

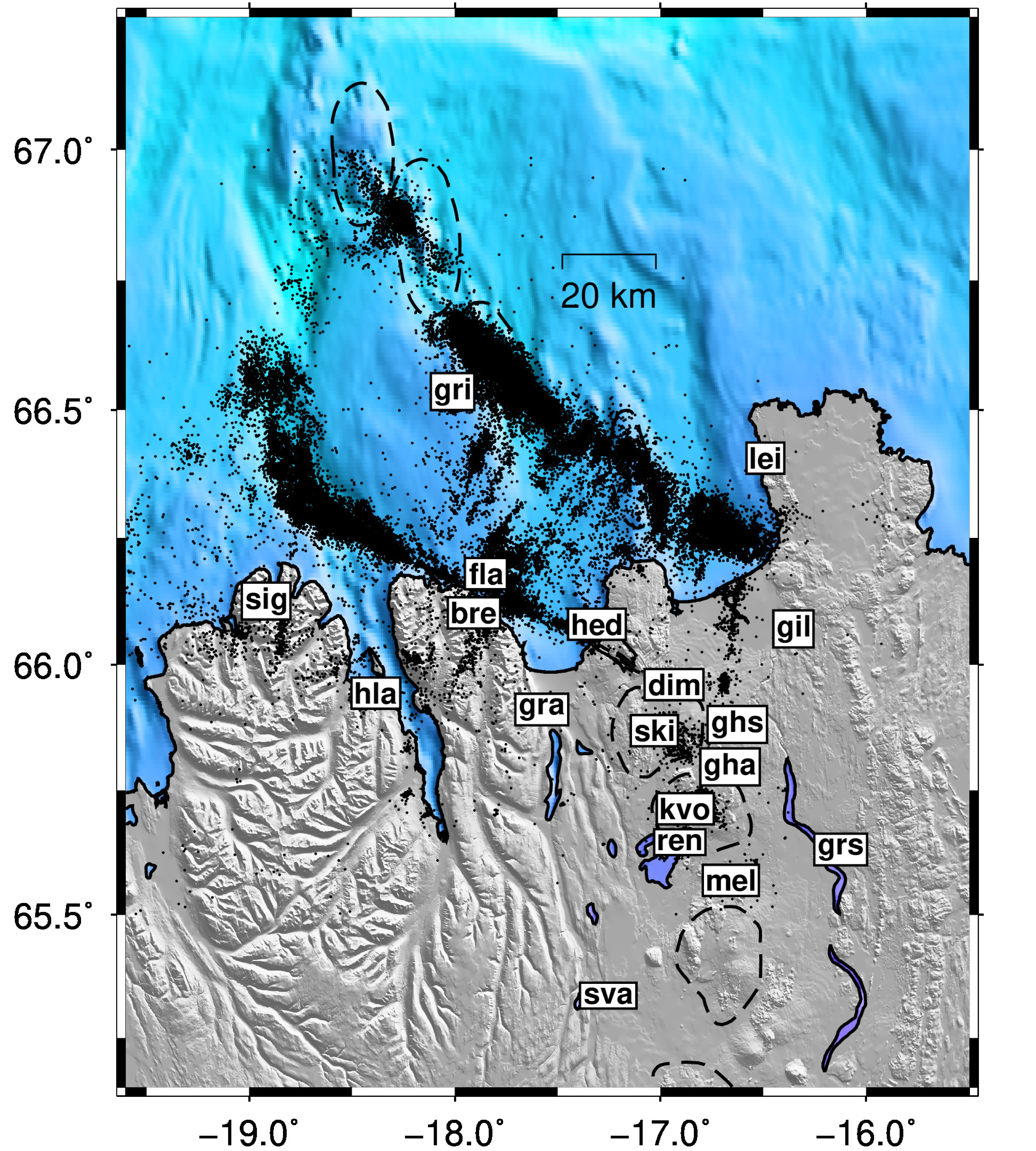
67.0°
66.5°
66.0°
65.5°
−19.0°
−18.0°
−17.0°
−16.0°
20 km
gri
lei
fla
sig
bre
hed
gil
hla
gra
dim
ski
ghs
gha
kvo
ren
grs
mel
sva

Figure 3.

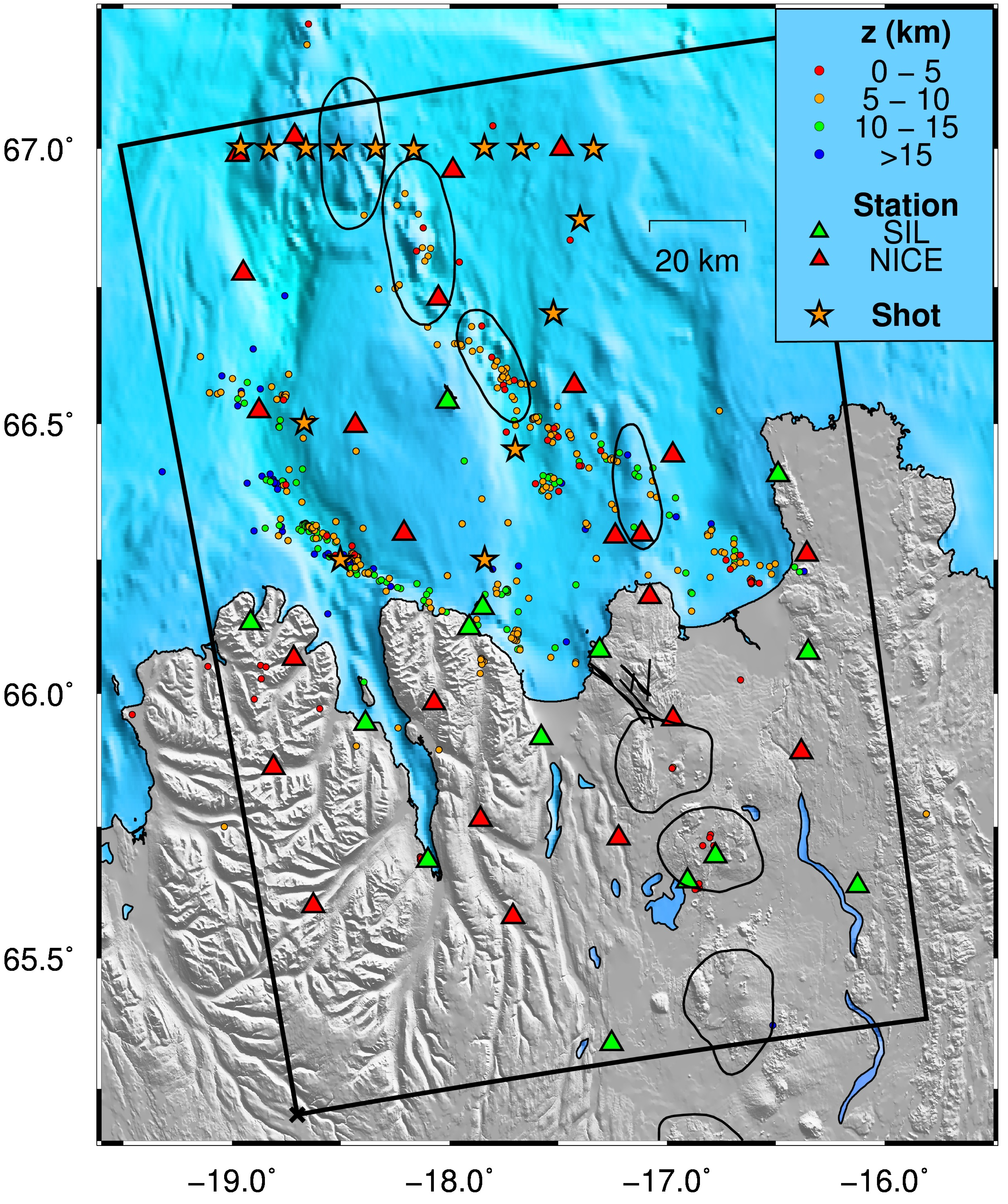
z (km)
0 – 5
5 – 10
10 – 15
>15
Station
SIL
NICE
Shot
20 km
67.0˚
66.5˚
66.0˚
65.5˚
−19.0˚
−18.0˚
−17.0˚
−16.0˚

Figure 4.

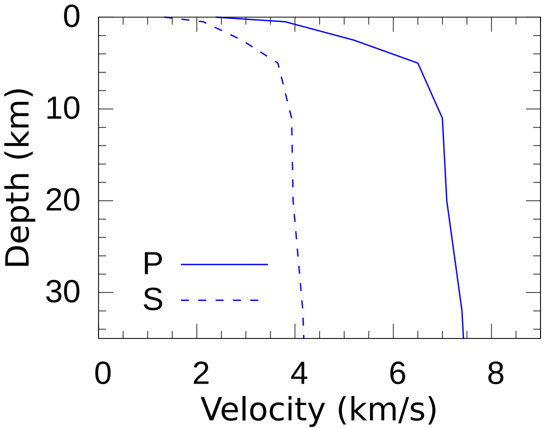

Depth (km)
0
10
20
30
Velocity (km/s)
0
2
4
6
8
P
S

Figure 5.

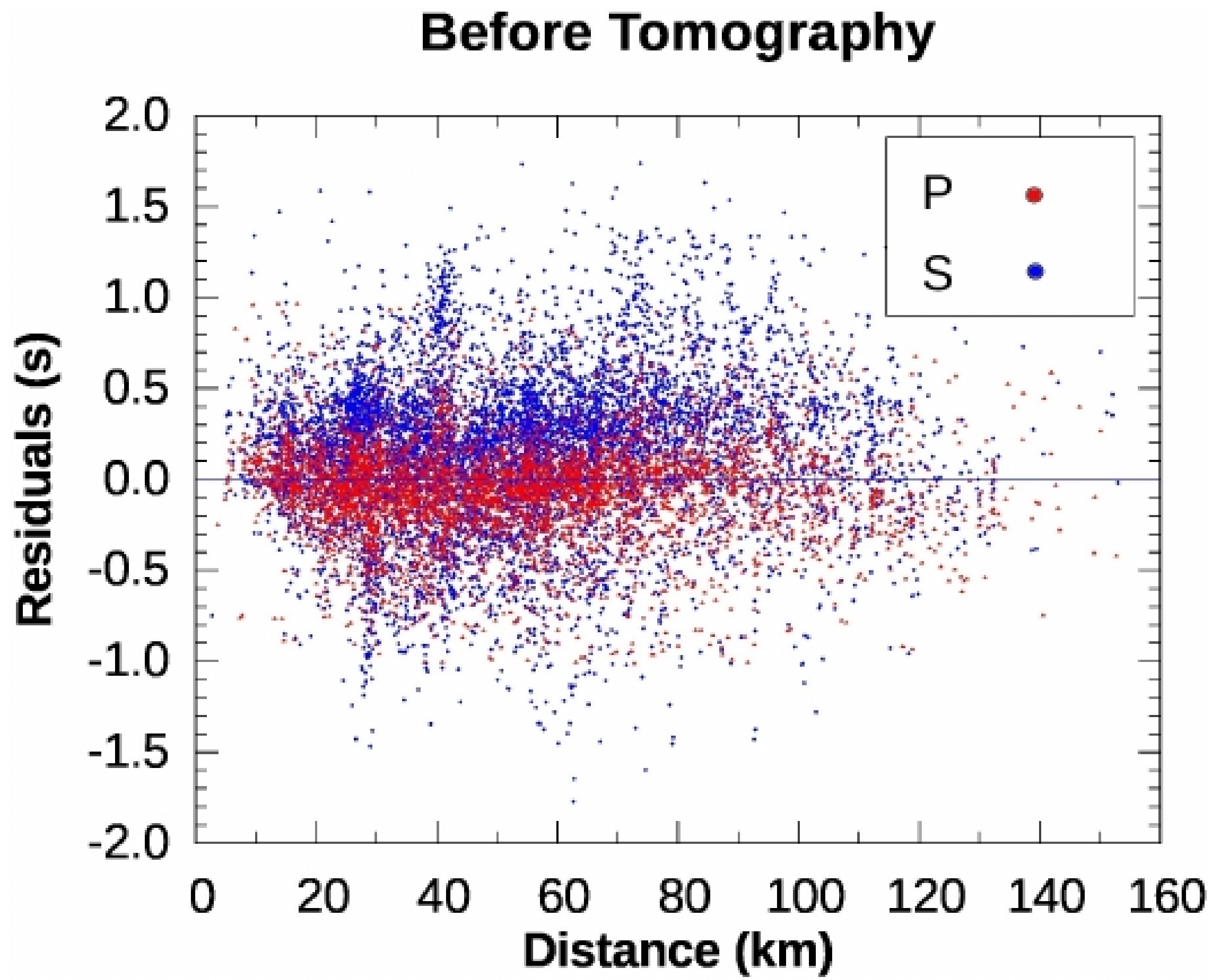

Before Tomography
Residuals (s)
Distance (km)
P
S
2.0
1.5
1.0
0.5
0.0
-0.5
-1.0
-1.5
-2.0
0
20
40
60
80
100
120
140
160

(a)

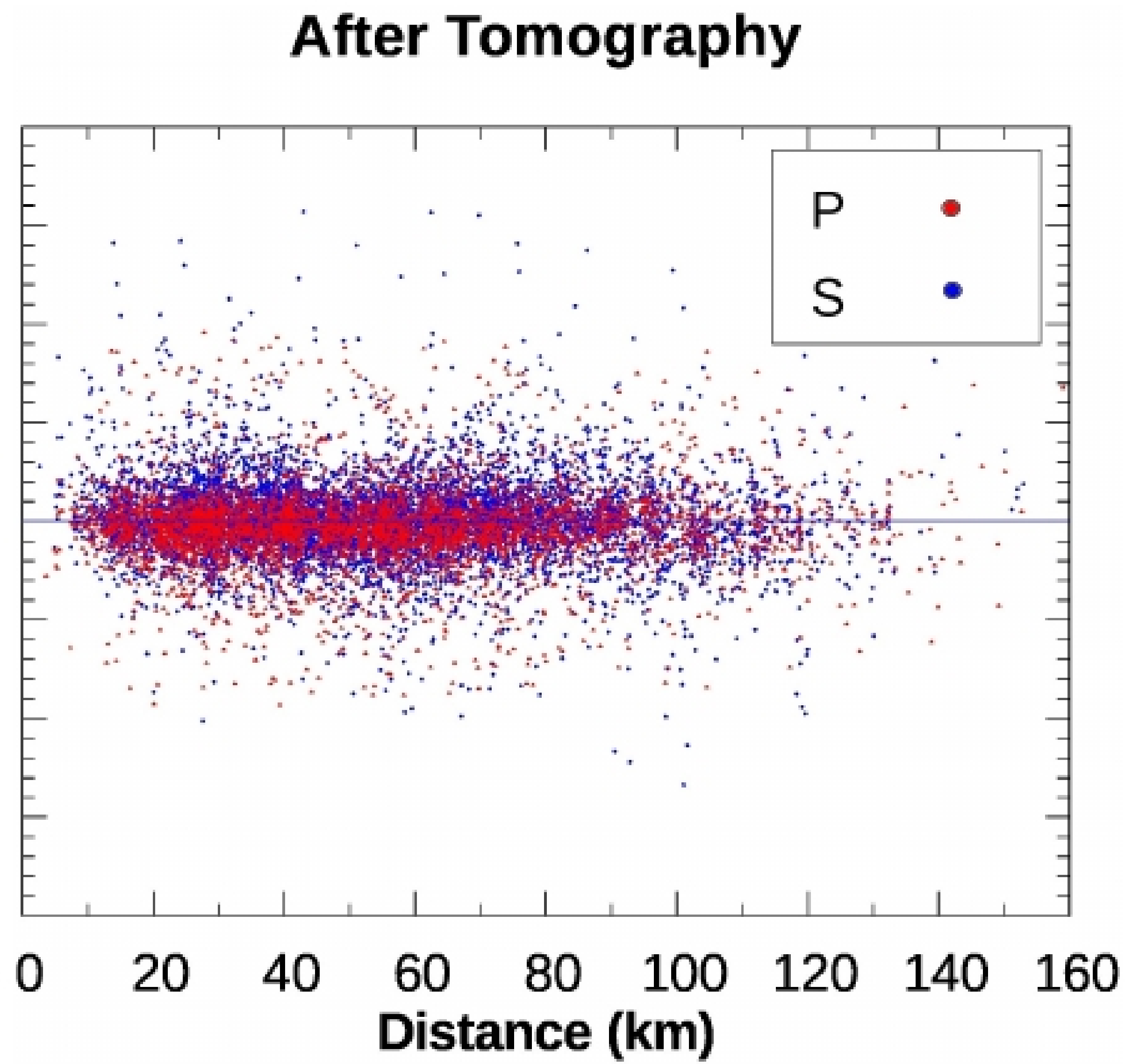

After Tomography
Distance (km)
P
S
0
20
40
60
80
100
120
140
160

(b)

Figure 6.

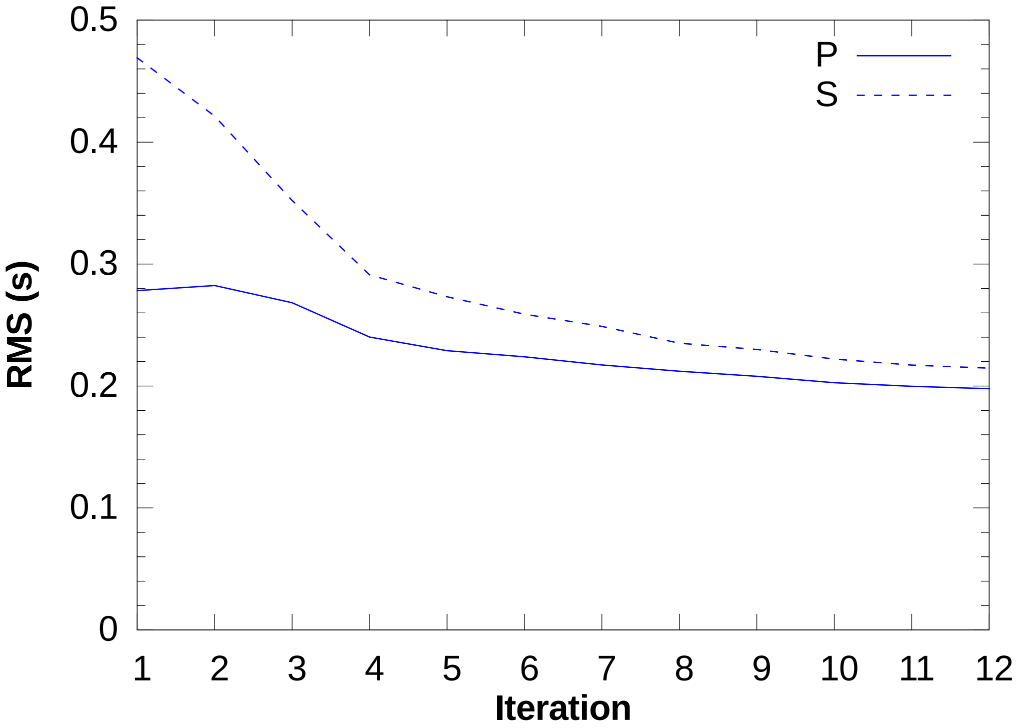

P
S
0.5
0.4
0.3
0.2
0.1
0
RMS (s)
1
2
3
4
5
6
7
8
9
10
11
12
Iteration

Figure 7.

X (km)
Z (km)
Y (km)
Z (km)
20 km
0
25
50
75
100
125
150
175
200
10
20

Figure 8.

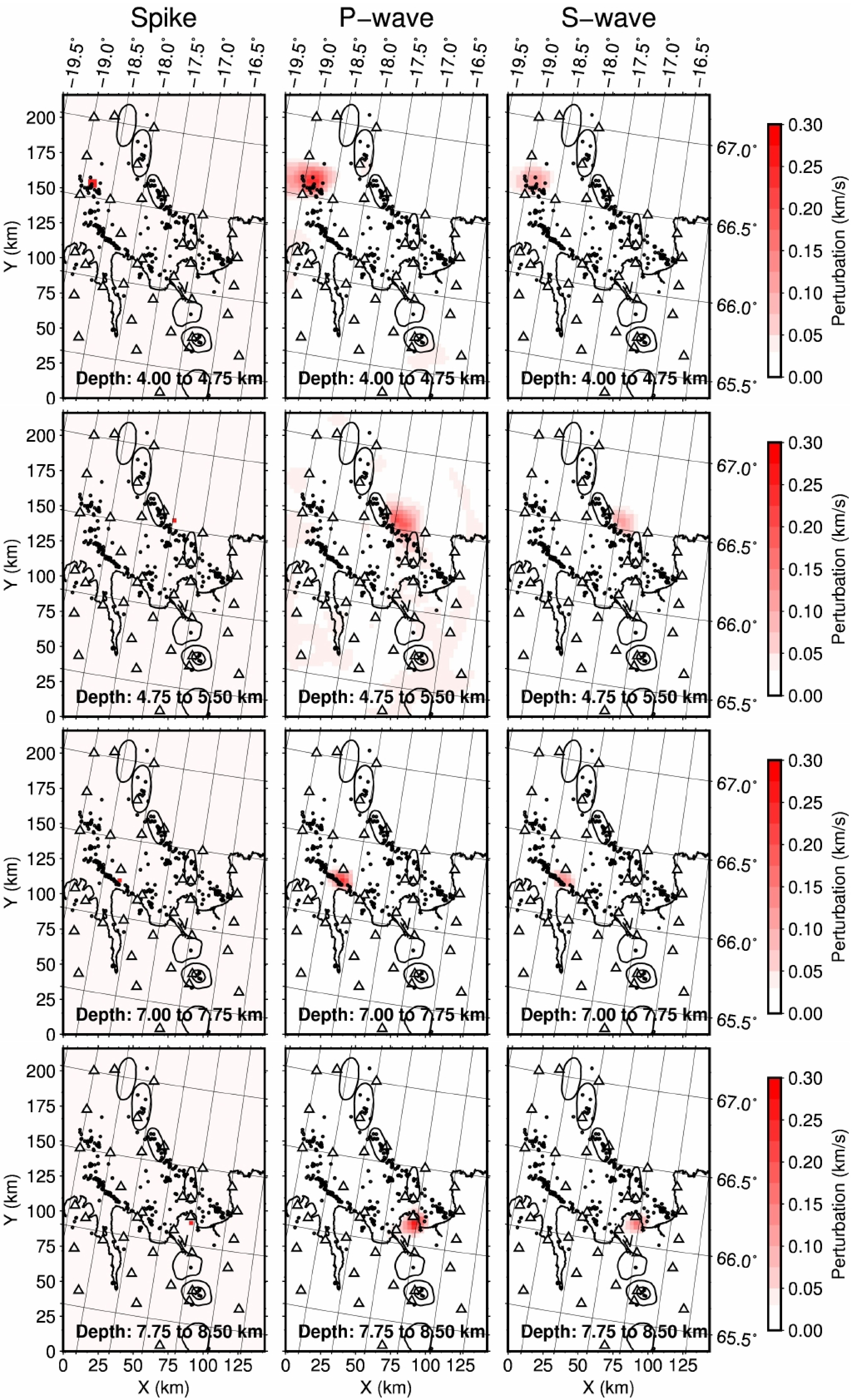
Spike
P−wave
S−wave
−19.5°
−19.0°
−18.5°
−18.0°
−17.5°
−17.0°
−16.5°
67.0°
66.5°
66.0°
65.5°
Y (km)
X (km)
Perturbation (km/s)
0.00
0.05
0.10
0.15
0.20
0.25
0.30
Depth: 4.00 to 4.75 km
Depth: 4.75 to 5.50 km
Depth: 7.00 to 7.75 km
Depth: 7.75 to 8.50 km

Figure 9.

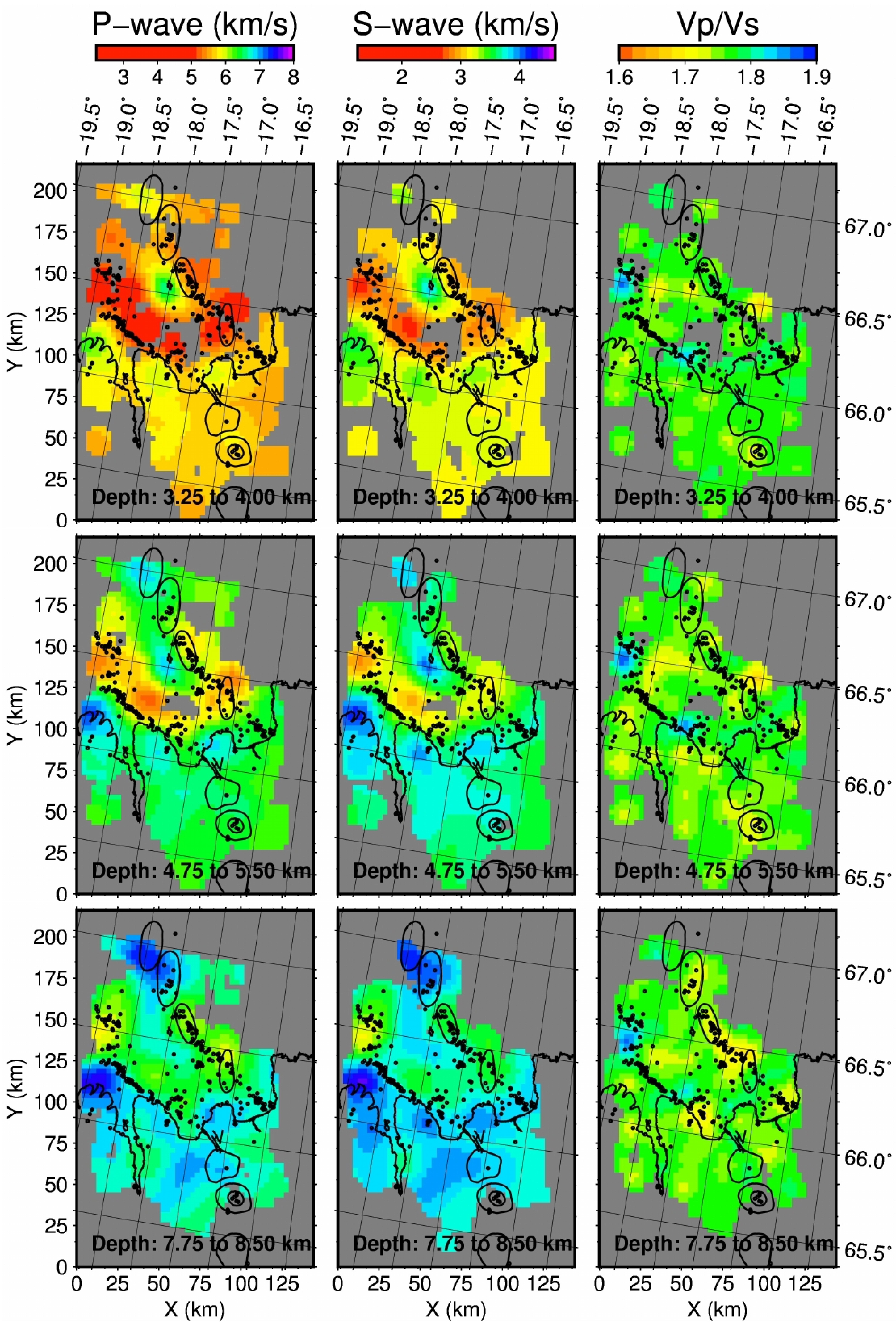

P−wave (km/s)
3 4 5 6 7 8
S−wave (km/s)
2 3 4
Vp/Vs
1.6 1.7 1.8 1.9
−19.5° −19.0° −18.5° −18.0° −17.5° −17.0° −16.5°
67.0° 66.5° 66.0° 65.5°
Y (km)
X (km)
Depth: 3.25 to 4.00 km
Depth: 4.75 to 5.50 km
Depth: 7.75 to 8.50 km

Figure 10.

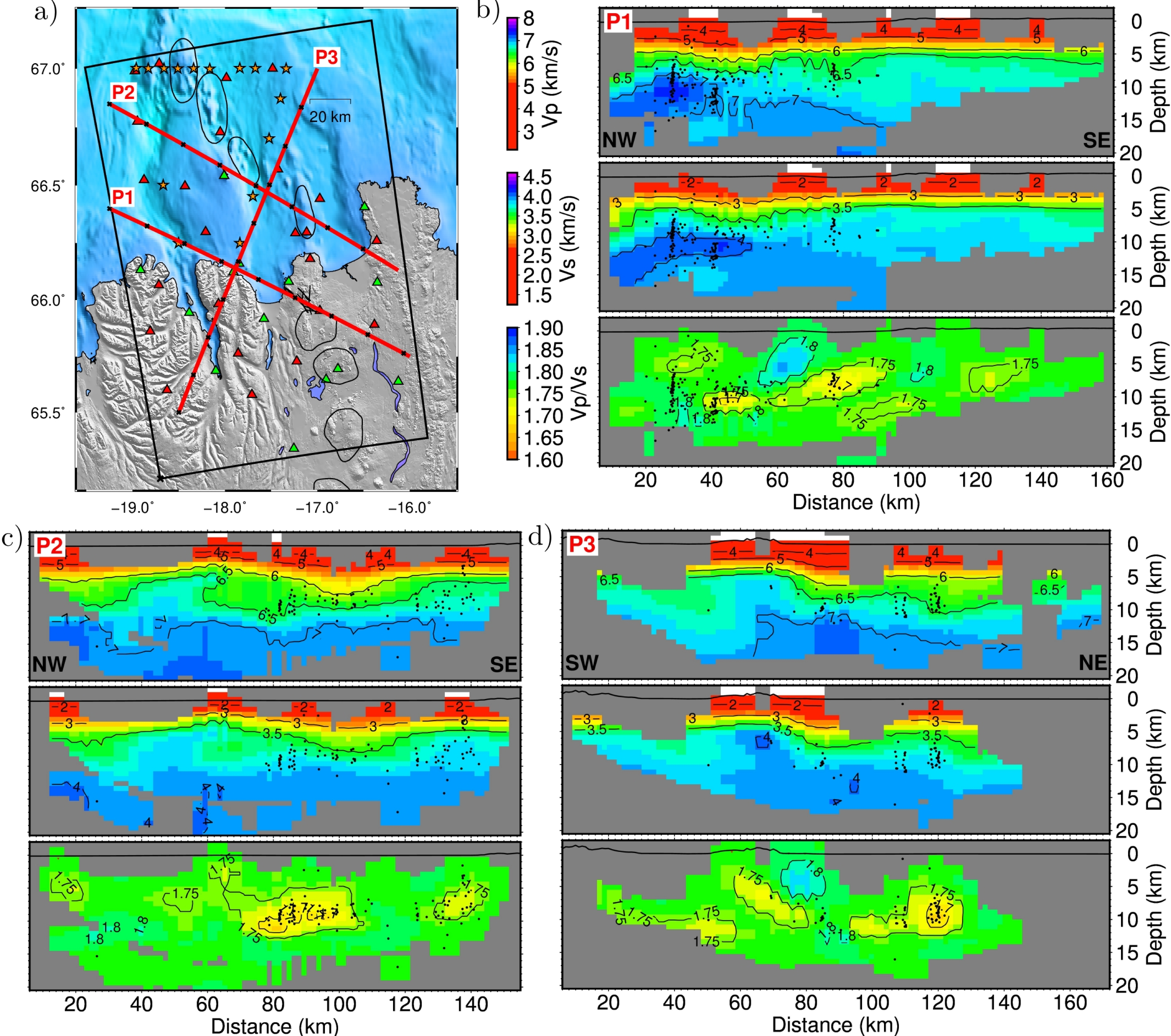

a)
b)
c)
d)
P1
P2
P3
20 km
67.0°
66.5°
66.0°
65.5°
−19.0°
−18.0°
−17.0°
−16.0°
Vp (km/s)
Vs (km/s)
Vp/Vs
NW
SE
SW
NE
Depth (km)
Distance (km)

Figure 11.

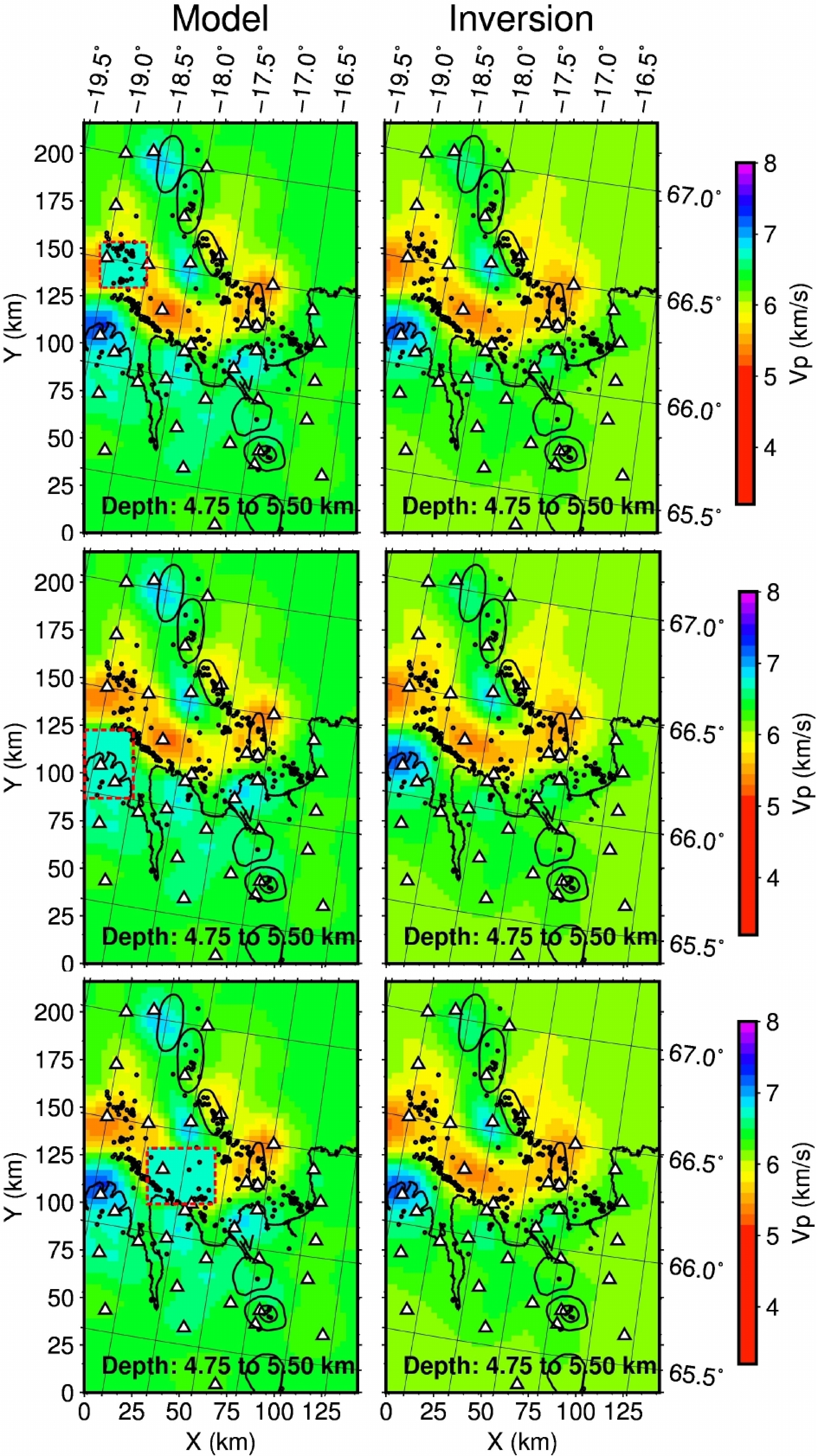

Model
Inversion
−19.5°
−19.0°
−18.5°
−18.0°
−17.5°
−17.0°
−16.5°
67.0°
66.5°
66.0°
65.5°
Y (km)
X (km)
Vp (km/s)
Depth: 4.75 to 5.50 km

Figure 12.

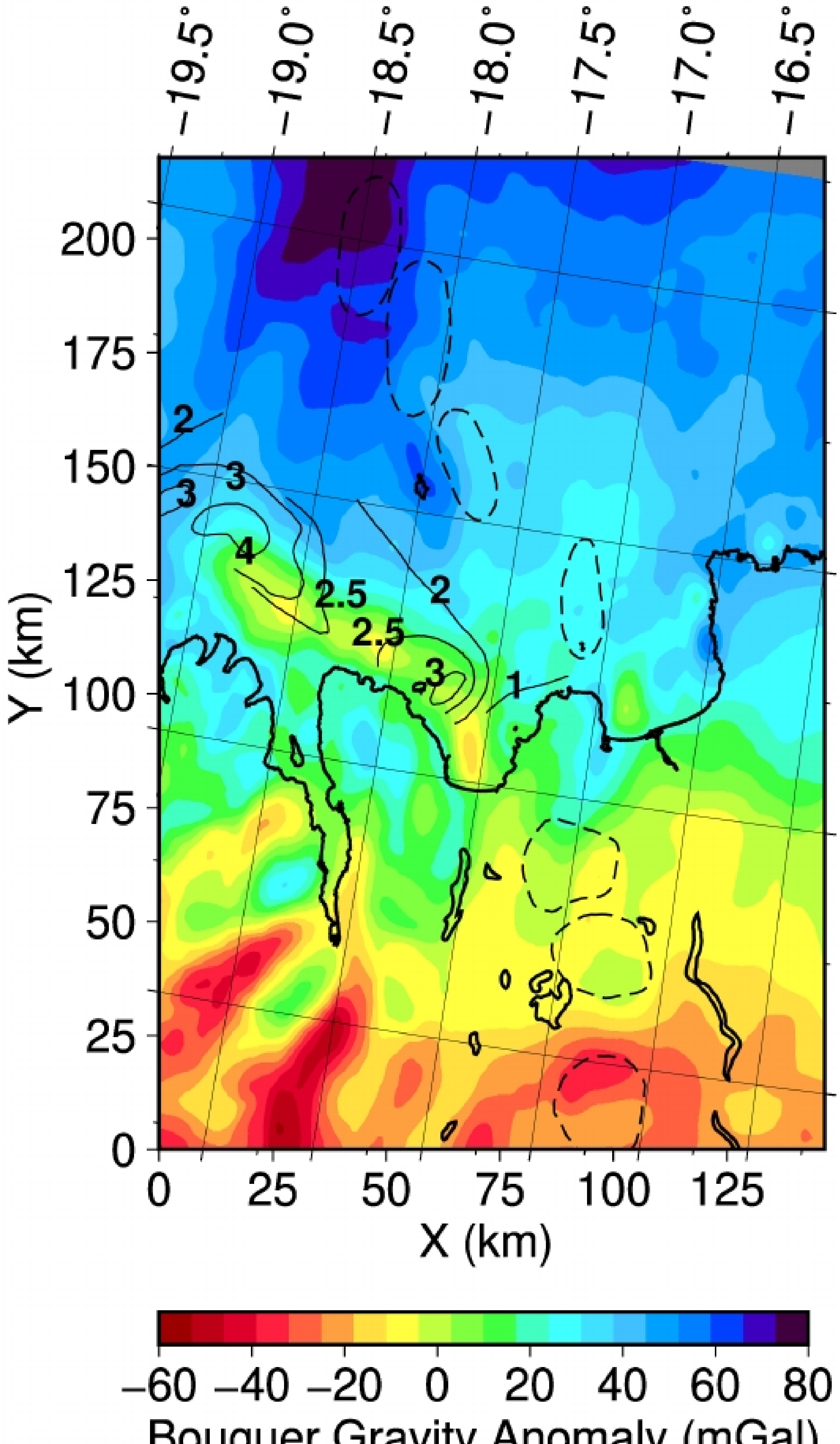
−19.5°
−19.0°
−18.5°
−18.0°
−17.5°
−17.0°
−16.5°
Y (km)
0
25
50
75
100
125
150
175
200
X (km)
2
3
3
4
2.5
2.5
2
3
1
−60
−40
−20
0
20
40
60
80
Bouguer Gravity Anomaly (mGal)

(a)

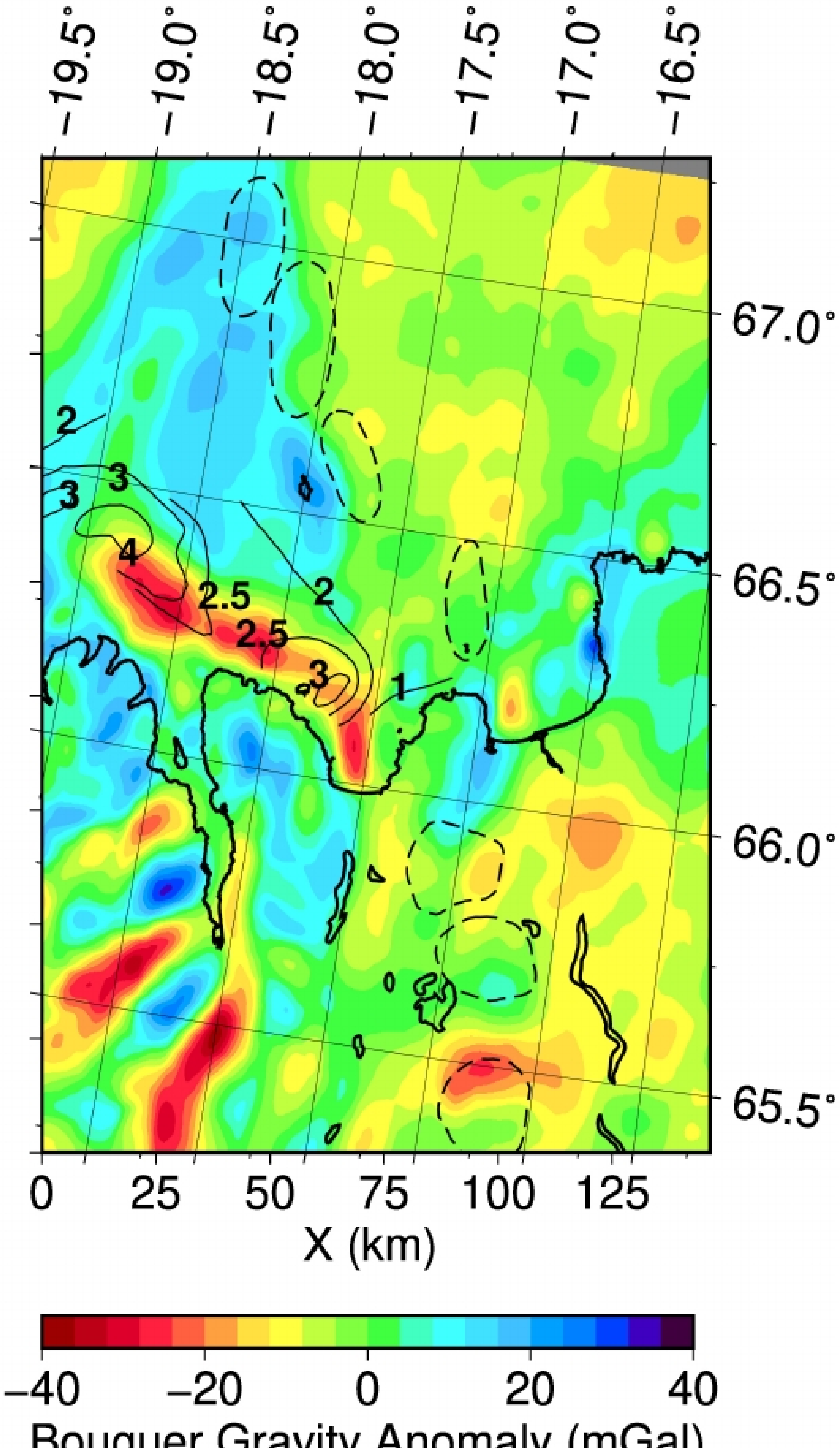
−19.5°
−19.0°
−18.5°
−18.0°
−17.5°
−17.0°
−16.5°
67.0°
66.5°
66.0°
65.5°
X (km)
0
25
50
75
100
125
2
3
3
4
2.5
2.5
2
3
1
−40
−20
0
20
40
Bouguer Gravity Anomaly (mGal)

(b)